Spatio-temporal variation of radionuclide dispersion from nuclear power plant accidents using FLEXPART ensemble modeling

S. Omid Nabavi[1], Theodoros Christoudias[1], Yiannis Proestos[1], Christos Fountoukis[2], Huda Al-Sulaiti[2], Jos Lelieveld[1,3]

[1]Climate & Atmosphere Research Centre, the Cyprus Institute, Nicosia, 2121, Cyprus (o.nabavi@cyi.ac.cy)
[2]Qatar Environment and Energy Research Institute (QEERI), Hamad Bin Khalifa University, Doha, Qatar
[3]Max Planck Institute for Chemistry, Mainz, 55128, Germany

Correspondence to: S. Omid Nabavi[1] (o.nabavi@cyi.ac.cy)

Abstract.

We estimate the seasonal and diurnal changes in the transport and intensity of radionuclides including Iodine-131 (^{131}I) and Cesium-137 (^{137}Cs), transported to Qatar from a fictitious accident at the Barakah nuclear power plant (B-NPP) in UAE. For dispersion modeling, we have used the Lagrangian particle/air parcel dispersion model FLEXible PARTicle (FLEXPART) driven by forecast and (re)analysis products, and coupled with the Weather Research and Forecasting model (FLEXPART-WRF). A four-member ensemble of meteorological inputs, including one forecast dataset (CFSv2) and three (re)analysis datasets (native resolution and downscaled FNL and downscaled ERA5), is used to force FLEXPART/FLEXPART-WRF. According to the age spectrum of Lagrangian particles, radionuclides entered southern Qatar about 10 to 20 hours after emission. Most of radionuclide transport and deposition in the study area occurred in less than 80 hours ~~, and almost all emitted particles are transported to and/or deposited in the study area within the 80 hours~~ after the release. A higher number of long-lived particles was found in FNL simulations and when particles are released in the afternoon and spring. The highest levels of simulated ^{131}I concentrations and ^{137}Cs deposition were found in FNL simulations in the south/southeast of Qatar. The frequent coincidence of high radionuclide concentrations and deposition with particles released between 5 a.m. and 2 p.m. and in the cold period of the year was attributed to diurnal and seasonal changes in the planetary boundary layer height (PBLH) and synoptic circulations. The difference in input PBLH explains well the inter-member variations of simulated radionuclide concentrations. Simulated concentrations were found with the same level of consistency as reported for real case studies.

1 Introduction

Modeling the spatio-temporal distribution of radioactive materials through chemical transport models (CTMs), especially after major nuclear events, has received widespread attention (Chino et al., 2011, Stohl et al., 2012, Christoudias and Lelieveld, 2013, Evangeliou et al., 2017). Whether explicitly stated or implied, all these studies seek to determine the magnitude and transport of radionuclides at different spatial scales. Such research activities help to improve the performance of CTMs as the core of preparedness programs for potential nuclear accidents (or releases) related to the increasing number of nuclear facilities (Farid et al., 2017). However, case studies of real accidents of the order of a few days are not suited to examine the impact of seasonal (atmospheric) changes on the radionuclide dispersion. For instance, Long et al. (2019) studied the effect of the East Asian northeast monsoon on the transport of radionuclides from the Fukushima nuclear power plant accident to the tropical western Pacific and Southeast Asia. They found that these regions received lower airborne radioactivity than other regions in the northern hemisphere due to the late arrivals of radionuclide plumes carried by the monsoon circulations. That is, the dispersion of radionuclides significantly differs under various atmospheric conditions. Maurer et al. (2018) found that the performance of dispersion models is largely dependent on successfully capturing boundary layer processes that vary in seasons and times of the day. In addition, the meteorological inputs of CTMs are produced by atmospheric models that in some cases exhibit variability when simulating atmospheric conditions over nuclear accident areas (Arnold et al., 2015). This is mainly due to the differences in their initial conditions, spatial and temporal resolutions, mathematical formulation, physical parameterization, etc.

Using an ensemble of meteorological inputs, this study primarily aims to investigate the seasonal and diurnal changes in the transport and surface concentration and deposition magnitude of radionuclides in the event of a potentially possible nuclear accident. Two radioactive tracers including Iodine-131 (^{131}I) and Cesium-137 (^{137}Cs) are assumed to be released from a fictitious accident at the Barakah nuclear power plant (B-NPP) in the UAE. Both radionuclides are emitted as gas, but due to lower volatility, ^{137}Cs condenses onto aerosol particles shortly after the release (Christoudias and Lelieveld, 2013). The relatively long half-life of ^{137}Cs (about 30 years), compared to ^{131}I (about 8 days), gives significance to the amount of ^{137}Cs that undergoes surface deposition and to ^{131}I concentration in the biosphere (Tsuruta et al., 2019, Takagi et al., 2020, Kinase et al., 2020, Wai et al., 2020). For dispersion modeling, we use the Lagrangian particle model FLEXible PARTicle (FLEXPART) (Stohl et al., 1998, Stohl et al., 2005, Brioude et al., 2013). The Eulerian CTMs model the transport of air pollutants by solving numerically the equation for the conservation of mass (Moussiopoulos, 1997, Zhang and Chen, 2007) which is computationally expensive (Brioude et al., 2013). Furthermore, in an Eulerian model, a particle released from a point source loses its position in the grid-box (numerical diffusion). Lagrangian particle dispersion models (LPDMs) instead have minimal numerical diffusion as they accurately model the trajectory of each particle individually (Nabi et al., 2015). Furthermore, LPDMs are more computationally efficient for particle dispersion modeling because these models calculate the advection and diffusion only for the location of each particle rather than for the entire model domain. However, LPDMs also have limitations. They suffer from numerical errors when interpolating meteorological fields in space and time. In some cases,

due to the lack of accuracy required to simulate the stochastic motion of particles and/or because the vertical velocity is not very precisely mass balanced with horizontal winds, particles may not remain well-mixed during the simulation (Brioude et al., 2013). Regardless of which type of CTM is being deployed, Girard et al. (2016) showed that uncertainties in meteorological fields, namely wind speed and direction and precipitation, and emission rate substantially contribute to errors in dispersion modeling. The three common methods for sensitivity analysis of LPDM simulations to meteorological information are: i) creating perturbations in the horizontal and vertical location of particles, ii) using a single meteorological model with perturbations to the initial conditions and/or model physics, and iii) using a suite of different meteorological models (Galmarini et al., 2004). By adopting the third approach, we used a four-member ensemble in which the performance of the forecast member, forced by 6-hourly data from NCEP climate forecast system version 2 (CFSv2), is compared against the (re)analysis members. (Re)analysis-based simulations are expected to be closer to (unavailable in a real-world scenario) actual values than forecast-based ones (Leadbetter et al., 2022). Two (re)analysis members are forced by dynamically downscaled meteorological inputs to study the effect of downscaling on FLEXPART dispersion modelling. We also studied the sensitivity of simulations regarding the choice of turbulence schemes under convective conditions. To study pollution risks for local communities, the radionuclide simulations were examined in relation to the population densities of the catchment region of interest (Qatar). To the best of our knowledge, this is the first time that such a study is conducted for potential radionuclide releases in the study region, and we expect that our results can contribute to the formulation of preparedness plans. The paper proceeds as follows: Section 2 outlines the LPDM, meteorological inputs, study area, and source term of radionuclides used in this study. Results are presented and discussed in Section 3. The study conclusions are given in Section 4.

2 Ensemble model configuration

We have used FLEXPART and FLEXPART driven by the Weather Research and Forecasting (FLEXPART-WRF) model for the dispersion modeling of ^{131}I and ^{137}Cs, fictitiously released from the B-NPP. The following is a brief description of the FLEXPART modeling structure.

2.1 FLEXPART and FLEXPART-WRF dispersion modelling

The details of the FLEXPART and FLEXPART-WRF modeling are available in Stohl et al. (2005) and Brioude et al. (2013), respectively. This subsection only discusses the principles of FLEXPART modeling that facilitate the presentation of results in the next section. FLEXPART, as a LPDM, is developed based on the zero acceleration scheme (Eq. 1). It solves a Langevin equation (Eq. 2) for modeling the trajectories of Lagrangian particles. The new location of particles is under the influence of large-scale winds, local turbulence (stochastic component), and mesoscale motions.

$$X(t + \Delta t) = X(t) + v(X, t)\Delta t \quad (1)$$

$$\frac{dX}{dt} = v[X(t)]$$

where t is time, Δt is the time increment, X is the position vector, and $v = \bar{v} + v_t + v_m$ the wind vector that is composed of the grid-scale wind $\bar{v}$, the turbulent wind fluctuations v_t and the mesoscale wind fluctuations v_m. FLEXPART also quantifies changes to the mass, or mixing ratio, of advected particles by computing various removal processes (Stohl and Thomson, 1999, Cassiani et al., 2015, Tipka et al., 2020). Turbulent motions v_{t_i} for wind components i are parameterized assuming a Markov process based on the Langevin equation (Eq. 2).

$$dv_{t_i} = \alpha_i(x, v_t, t)dt + b_{ij}(x, v_t, t)dW_{j} \quad (2)$$

Where α is the drift term, b the diffusion term, and dW_{j} incremental components of a Wiener process with mean zero and variance dt, which are uncorrelated in time (Stohl et al., 2010). The minimum value of Δt_i is 1 second. Δt_i is used only for the horizontal turbulent wind components of Eq. 2.

$$\Delta t_i = \frac{1}{ctl} min(\Delta\tau_{L_\omega}, \frac{h}{2\omega}, \frac{0.5}{\frac{\partial\sigma_\omega}{\partial z}}) \quad (3)$$

where h is the height of the atmospheric boundary layer (ABL). For solving the Langevin equation for the vertical wind component, a shorter time step $\Delta t_\omega = \frac{\Delta t_i}{ifine}$ is used. Under convective conditions, when turbulence is skewed, larger areas are occupied by downdrafts (rather than updrafts). This may lead to higher surface concentrations (deposition) in areas neighboring the pollution sources (Pisso et al., 2019). To investigate the sensitivity of radionuclide magnitudes to the used turbulence scheme, FLEXPART-WRF members were rerun after replacing the default Gaussian turbulence model (GTM) with the skewed turbulence model (STM) (Luhar et al., 1996, Cassiani et al., 2015)~~((Luhar et al., 1996, Cassiani et al., 2015) and Cassiani et al. (2013))~~. The output of either of these schemes is used for the computation of the vertical velocity component of the drift term in Eq. 2. The implementation of STM requires shorter time steps, dt in Eq. 2, to better resolve turbulence in the convective planetary boundary layer. Hence, we used a tenfold finer time step, as recommended by Pisso et al. (2019), in sensitivity runs. For the computation of σ_{v_i} and $\Delta\tau_{L_i}$, FLEXPART uses the parameterization scheme proposed by (Hanna, 1982). In order to take mesoscale motions (v_m, in Eq. 2) into account, a similar method as Maryon (1998) is followed.

In dispersion modeling, particle mass reduction mainly occurs through three processes: radioactive decay, dry deposition, and wet deposition. The following exponential equations characterize the radioactive decay (Eq. 4) and wet deposition (Eq. 5).

$$m(t + \Delta t) = m(t)exp(-\Delta t/\beta) \quad (4)$$

where m is particle mass, and the time constant $\beta = \frac{T_{\frac{1}{2}}}{\ln(2)}$ is determined from already calculated the radionuclide half-life $T_{\frac{1}{2}}$.

$$m(t + \Delta t) = m(t)exp(-\Lambda\Delta t) \quad (5)$$

The scavenging coefficient Λ is calculated differently depending on whether the particle in question is in the aerosol or gas phase and whether scavenging takes place inside or below clouds (Stohl et al., 2005).

In this study, we have used FLEXPART 10.4 and a modified version of FLEXPART 9.02 to ingest meteorological simulations from the Weather Research and Forecasting (WRF) (Grell et al., 2005) (Hereafter referred to as FLEXPART and FLEXPART-WRF, respectively). Compared to previous versions, FLEXPART has undergone a significant revision in the calculation of wet deposition. In recent updates~~(Grythe et al., 2017)~~, the dependency of wet deposition on the size of aerosol particles and the type of precipitation has been considered (Grythe et al., 2017). In addition, FLEXPART only calculates wet deposition for cloudy pixels in which the precipitation rate exceeds 0.01 mm h^{-1}. Therefore, the accuracy of cloud pixel detection plays a critical role in the accuracy of location and amount of wet deposition simulated by FLEXPART. In the previous versions (including version 9.02 used in the development of FLEXPART-WRF 3.2), in-cloud grid cells were defined as those with relative humidity above 80% and any grid cells beneath these grid cells as below-cloud ones (Seibert and Arnold, 2013). Because of recent updates, FLEXPART now uses 3D fields of cloud water mixing ratio and the relative fractions of ice and liquid water (type of precipitation). Therefore, it is expected that part of the difference between FLEXPART and FLEXPART-WRF simulations in the wet period of the year is due to the differences in the schemes used to calculate the scavenging. Pisso et al. (2019) have discussed these and other updates in the recent version of FLEXPART in more detail. Regarding dry deposition, for all particles below two times the reference height (h_{ref}), the particle mass reduction is calculated by using Eq. 6:

$$\Delta m(t) = m(t)[1 - exp\left(\frac{-v_d(h_{ref})\Delta t}{2h_{ref}}\right)] \quad (6)$$

v_d is the dry deposition velocity that is calculated as the ratio of $v_d(z) = \frac{F_C}{C(z)}$ for the h_{ref} of 15 m. F_C and C are the flux and the concentration of a species at height z within the constant flux layer. If the necessary information for the parameterization of dry deposition of gases and particles is not available, v_d can be assumed constant. The concentration of a given gas or aerosol species in a grid cell is equal to the weighted average of total particle mass within the grid cell divided by the grid cell volume (Pisso et al., 2019) as defined in Eq.7.

$$C(z) = \frac{1}{v}\sum_i^N (m_i f_i) \quad (7)$$

with V being the grid cell volume, m_i particle mass, N the total number of particles, and f_i the fraction (weight) of the mass of particle i attributed to the respective grid cell. The amount of dry and wet deposition for the grid cell i is by default accumulated over the model time dimension unless the age composition of air parcels is required as was the case in this study. A unique feature of FLEXPART/FLEXPART-WRF is the grouping of simulations based on the age of Lagrangian particles. This means that the number of concentrations and deposition in each time step is obtained from the aggregation of the simulations through the added dimension of particle ages. In this study, we used the age spectrum of Lagrangian particles to estimate the transport of radioactive materials from source to receptors. ~~We use the terms transport and Lagrangian particle/air parcel age interchangeably in the rest of the paper.~~ The age of air parcels was examined in an hourly resolution. As a result, a new dimension with a size of 96 (hours) is added to the history output grids that have a horizontal resolution of 10 km in 14 vertical levels from 5 to 5000 m agl. For the one-by-one comparison of age distributions of air parcels from ensemble members, we

have used the maximum normalized difference as defined in Eq. 8. Assuming that a and b are two distributions of smooth density estimates of air parcel ages, their normalized difference is defined as the maximum value of the absolute differences of these two distributions divided by the maximum value of these two distributions. Higher values of this metric indicate greater differences in distributions (Jin and Kozhevnikov, 2011).

$$\text{maximum normalized difference} = \frac{\max(\text{abs}(a-b))}{\max(\max(a), \max(b))} \quad (8)$$

~~While m~~Modeled concentrations ~~(subsection 3.3)~~ are vertically integrated through all model levels in analyses related to air parcel ages (subsection 3.1) and inter-member evaluation (subsection 3.3)~~.~~ The thickness-weighted averages of simulations in the lowest four model levels between 5 and 100 m agl (with layer thicknesses of 5 m, 5 m, 40 m, and 50 m) are used for the spatial analysis (subsection 3.2).

2.2 Meteorological data

FLEXPART/FLEXPART-WRF runs in offline mode with grid-scale meteorological fields from numerical weather prediction models. In this study, we obtained meteorological inputs from NCEP climate forecast system version 2 (CFSv2) (Saha et al., 2011, Saha et al., 2014), the NCEP final analysis (FNL) (NCEP, 2015), and the ECMWF reanalysis 5th generation (ERA5) (Hersbach et al., 2020). CFSv2, which entered into the operational mode in March 2011, is a fully coupled climate model representing the interactions between the Earth's oceans, land, and atmosphere. CFSv2 can be used to provide 6-hourly forecast inputs for FLEXPART at the spatial resolution of 0.5 degrees from 2011 onward. FNL provides the three-hourly combination of analysis (at 00, 06, 12, and 18) and forecast meteorological fields (at 03, 09, 15, and 21) using the Global Data Assimilation System (GDAS). It is available at a spatial resolution of 0.25 degrees starting from 2015. ERA5, the successor to ERA-Interim, is the latest generation of ECMWF reanalysis data that covers from January 1, 1950, to nearly the present. They are produced at a spatial resolution of about 31 km at hourly time steps. CFSv2 and FNL are used as the inputs of FLEXPART. ERA5 and FNL analyses were first dynamically downscaled by WRF to ~~create~~ provide inputs for two downscaled members ~~ERA5- and FNL-WRF~~. Subsequently, they are fed into FLEXPART-WRF with the new spatial and temporal resolution of 10 km and hourly. To the best of our knowledge, this is the first time that ERA5 inputs are used for the implementation of FLEXPART-WRF.

An overview of the input data and corresponding simulation codes is presented in Table 1. A single simulation code is built for each meteorological dataset to be ingested by FLEXPART whereas the FLEXPART-WRF takes inputs via one common simulation code. Therefore, there are three independent simulation codes (in the second column in Table 1) for the four meteorological datasets used in this study.

Table 1 The summary of meteorological inputs used to run FLEXPART and FLEXPART-WRF. The abbreviated names of meteorological datasets are affixed to their corresponding simulation codes in the second column.

Formatted: Font: 11 pt, Complex Script Font: 14 pt
Formatted: Font: 11 pt, Complex Script Font: 11 pt
Formatted: Centered
Formatted: Font: 11 pt, Complex Script Font: 11 pt
Formatted: Font: 11 pt, Complex Script Font: 11 pt
Formatted: Font: 11 pt, Complex Script Font: 11 pt
Formatted: Font: 11 pt, Complex Script Font: 11 pt
Formatted: Font: 11 pt, Complex Script Font: 11 pt
Formatted: Font: 11 pt, Complex Script Font: 11 pt
Formatted: Font: 11 pt, Complex Script Font: 11 pt
Formatted: Font: 11 pt, Complex Script Font: 11 pt
Formatted: Font: +Headings (Times New Roman), Font color: Text 1, (Complex) Persian (Iran), English (United States)

Inputs	Simulation code	Spatial resolution	temporal resolution	time coverage	downscaled	tType of input	wet deposition scheme
CFSv2	FLEXPART_CFSv2	0.5 degrees	6-hourly	2011-present	X	forecast	Grythe et al. (2017)
FNL	FLEXPART_FNL/FLEXPART-WRF	10 km	hourly	2015-present	X/✓	analysis	Grythe et al. (2017)/Seibert and Arnold (2013)
ERA5	FLEXPART-WRF	10 km	hourly	1950-present	✓	reanalysis	Seibert and Arnold (2013)

Formatted: Font: 10 pt, Complex Script Font: 10 pt

Formatted Table

Field Code Changed

Field Code Changed

Field Code Changed

Field Code Changed

2.3 Emission scenario and study area

We have simulated a fictitious nuclear accident at the B-NPP (Fig. 1-A) during which 22 PBq (6.9 kg) of ^{137}Cs and 192 PBq (0.042 kg) of ^{131}I are released during the first 24 hours. These amounts are the upper bound of emissions that Babukhina et al. (2016) estimated for the Fukushima Daiichi nuclear accident in May 2011. We simulated a fictitious release of radioactivity at a level comparable to the Fukushima nuclear accident. However, our study does not replicate previous accidents or simulates a specific real-world case; rather we designed this analysis to determine what time of the day and year is associated with particular probabilities of transport of dense radionuclide plumes from any hypothetical release in the study area. A total number of 10^{45} Lagrangian particles were released almost uniformly during the emission period (~417 particles per hour). To choose the optimal number of particles, we have followed the literature (Papagiannopoulos et al., 2020, Thompson et al., 2015, Fast and Easter, 2006). The computational time scales linearly increase with the increasing number of particles, while the statistical error of simulations decreases with the square root of the particle density (Pisso et al., 2019). The particles are initially distributed at height levels between 100 and 300 m above the ground level over the emission point. Each simulation starts at the beginning of each day and lasts 96 hours i.e., 4 days (Fig. 1-B). This experiment has been performed for each day of 2019 leading to a total of 1460 simulation days (365 days of the year x 4 forward simulation days). For the diurnal and seasonal stratification of simulations, we always refer to the time when a particle is released (not to when it travels or reaches receptors). The simulation domain is bounded between 17°N-33°N and 40°E-60°E, and for post-processing, the geographical box over Qatar, from 24.25°N to 26.35°N and from 50.65°E to 51.75°E, has been analysed.

Formatted: Font: 10 pt, Not Bold, Not Italic, Font color: Auto, Complex Script Font: Not Bold, Not Italic, English (United States)

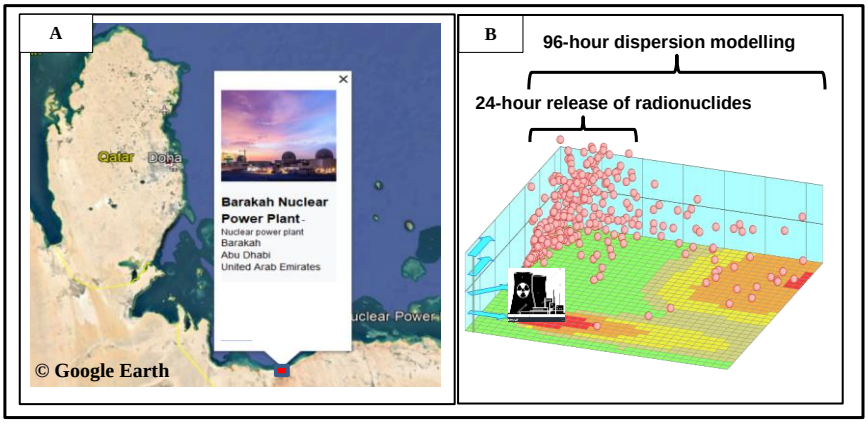

Figure 1 A is the study area embracing the B-NPP (red square) and the state of Qatar. The base map and overlaying information are taken from Google Earth. B is the schematic illustration of the LPDM simulation cycle. The original figure is available at https://www.janicke.de/en/lasat.html (last access: ~~4~~30 October~~May~~ 2022).

3 FLEXPART/FLEXPART-WRF simulations:

It should be noted that due to high solubility and the relatively long half-life of ^{137}Cs, further emphasis is placed on the spatio-temporal distribution of ^{137}Cs deposition. Conversely, the ambient surface-level concentration of ^{131}I over the study area will be considered since it resides mostly in the gaseous phase and has a short half-life of 8 days.

3.1 Diurnal and seasonal analysis of radionuclide transport

In order to investigate the diurnal and seasonal variations in the transport of radionuclides, we examined the simulated age of the Lagrangian particles entering the study area by the season and time of day in which they were released from B-NPP. The frequency density plots of air parcel ages for ^{131}I and ^{137}Cs are shown in Figures 2 and S1, respectively. The significant similarity of age distributions of ^{131}I and ^{137}Cs indicates that differences in the transport characteristics of these radionuclides, such as the wet and dry deposition rate and radioactive decay, are not large enough to cause the abundance of cases where ^{131}I and ^{137}Cs particles are not present in a common grid. The close dispersion of ^{131}I and ^{137}Cs concentrations, especially at low intensities, ~~(at least base concentrations)~~ and, consequently, the age of corresponding air parcels can be attributed to the lack of heavy precipitation in the region. This can be seen in S2 where a positively skewed distribution is found for the ratio of ^{137}Cs wet deposition to total ^{137}Cs deposition. Therefore, the following discussion related to the ages of particles simulating ^{131}I concentrations is also valid for ^{137}Cs concentrations (shown in the supplement). All ensemble members in all seasons simulated an abrupt increase (or a peak) in the number of air parcels with lifetimes of less than 20 hours (top row in Fig. 2-A).

Formatted: Complex Script Font: 10 pt

This indicates that, regardless of the time of year, radionuclide clouds started crossing the borders of the study area within a few hours after the emission. The maximum normalized distance of age distributions (Fig. 3) shows larger similarity between FNL-WRF and ERA5-WRF than between the former and FNL in all seasons other than the fall (0.3, 0.19, 0.25, and 0.38 vs. 0.3, 0.32, 0.32, and 0.41 in fall, spring, summer, winter). This may to be due to the use of meteorological inputs with the same spatio-temporal resolution and a common simulation code and, consequently, similar modeling schemes for the two former members. Although the base model used for the production of FNL, the Global Forecast System (GFS), is also the atmospheric component of CFSv2, the distribution differences were found to be lower between the FNL age distribution and those from ERA5- and FNL-WRF for most seasons.

In addition to having finer spatial resolution than CFSv2, FNL assimilates observations like ERA5. Compared to other members, air parcel ages are distributed in a wider range in all seasons in FNL (note the location of the first and last peaks). This could be because: FNL simulated 1- a decrease in transport speed to the same receptors and/or 2- a higher frequency of air parcels reaching further receptors from the source (discussed later). ~~, and/or 3- an increase in the residence time of air parcels over the same receptors. While the two former cases are examined in the next section, the study of air parcel residence time requires the calculation of source-receptor relationship (Seibert and Frank, 2004). The residence time of Lagrangian particles is outputted when FLEXPART and FLEXPART-WRF are executed in the backward mode (Pisso et al., 2019), which is beyond the scope of this study.~~

Formatted: Font: 9 pt, Bold, Complex Script Font: 9 pt, B (Complex) Persian (Iran)

To understand how the transport may change with the levels of radionuclide concentrations, beside the previous categorization, air parcel ages were separated into three levels representing low (the top row in S3-A), moderate (the bottom row in S3-A), and high (the bottom row in Fig. 2-A) concentrations of ^{131}I (see S1 and S4 for ^{137}Cs). These categories, for each member, are determined based on column (mass) densities, computed from the vertical integration of concentrations. The low, moderate, and high values are respectively lower than the 33rd percentile, between the 33rd and 66th percentiles, and greater than the 66th percentile. The strong positively skewed age distributions of particles that carried moderate (in the supplement) and high concentrations of both radionuclides in all members and all seasons indicate that they reach the study area boundaries within a few hours (less than 20 hours) after the accident. These results are to be expected as the southeast of the study area is very close to the source point (B-NPP). It is also worth mentioning that all members of the ensemble model (including the forecast member) have a greater agreement in air parcel ages for the moderate and high levels of ^{131}I and ^{137}Cs than those simulated for low concentrations. This is in line with the principles of FLEXPART dispersion modeling. According to Pisso et al. (2019), the error rate of simulations decreases with the square root of the particle density. As a result, all four members simulated the age of Lagrangian particles corresponding to moderate and high concentrations more closely and, most likely, more accurately near the source. For low intensities of both radionuclides, however, the age distributions are almost the same as that seen in all intensities.

The peak of newly arriving air parcels in all intensities occurs earlier in spring than in other seasons. There is also a delayed peak of long-lived air parcels in low and all intensity column densities in the spring. Therefore, it can be concluded that regional

atmospheric circulations led to the more distant transport of radionuclides to northern parts of the study area in this season than in other seasons. Figure 2-B (S1-B) shows the categorization of age distributions based on the release time of particles carrying ^{131}I (^{137}Cs) in the first 24 hours of each simulation period. This panel is similar to 2-A, but shows the age distributions plotted separately for particles released in 6-hour periods of the first day of the simulations. For example, the upper left figure shows the age distribution of the particles that is released within the first 6 hours of simulations.

This new categorization reveals that the number of long-lived air parcels (including all intensities of concentrations) increased in all members when particles are released between 12 and 6 p. m. (top row in Fig. 2-B and S1-B). This temporal pattern may be due to the coincidence of particle release and the development of the planetary boundary layer in the afternoon that caused the transport of radionuclides to longer distances, (represented by longer Lagrangian particle ages). Because particles that are released at the end of the day have less time to travel by the end of simulation period, a sharper fall is observed in the right tail of the age distributions during the second half of the day. However, the lifetime of most simulated particles, especially of those that caused moderate (bottom row in Fig. S3-B and S4-B) and high intensities (bottom row in Fig. 2-B and S1-B), is found to be between 20 and 70 hours after release. Consequently, the difference in release time of Lagrangian particles is not significantly affected by their age spectrum. Compared to ERA5-WRF and FNL-WRF, CFSv2 and FNL have simulated a larger number of shorter-aged air parcels after sunset (between 6 and 11 p.m.). It is because the spatio-temporal resolution of inputs used in these two members is too coarse to resolve the gradual reduction of boundary layer height resulting in fewer particles being transported to remote areas. Like seasonal distribution, the diurnal variations of air parcel ages for high concentrations are very similar in all members (bottom row in Fig. 2-B and S1-B). They all simulated a higher number of shorter-lived parcels when they are released in the first half of the day. Although a firm conclusion would require further studies at very-high-resolution of land-sea circulations in the region, onshore winds passing the emission point from the south may cause the abundance of shorter-lived parcels in southern Qatar.

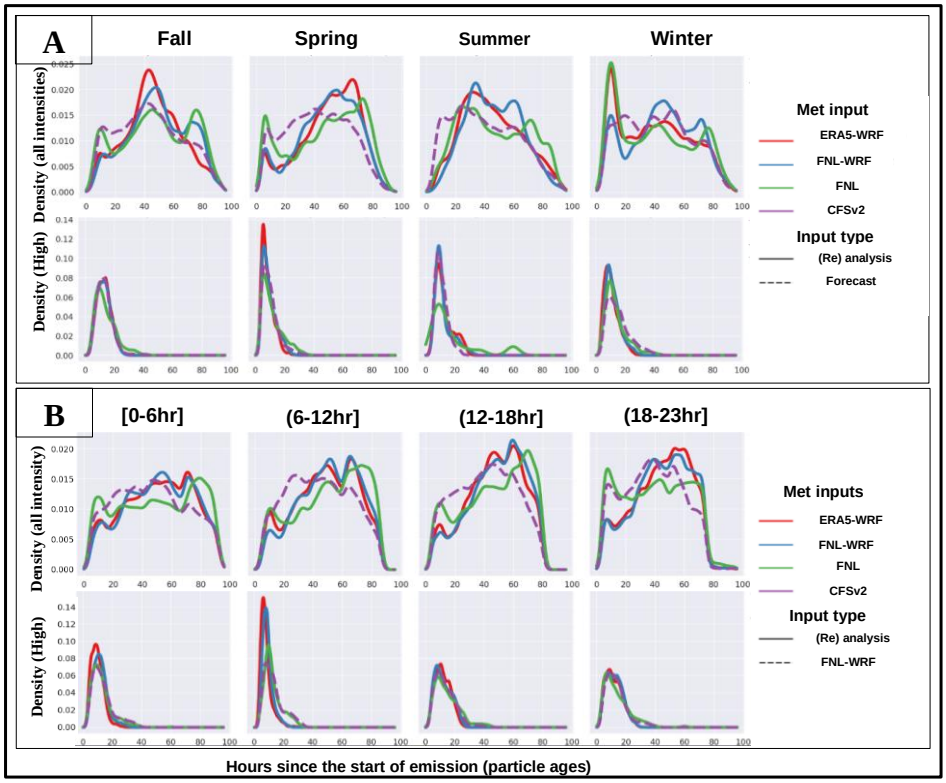

Figure 2 A: the smooth density estimates of air parcel ages corresponding to all intensities of ^{131}I column densities (top row) and of those above the 66th percentile (bottom row). B: the same as A, but for four times of the day. The curves represent simulations from each member of the ensemble. y-and x-axes show density values and air parcel ages, respectively.

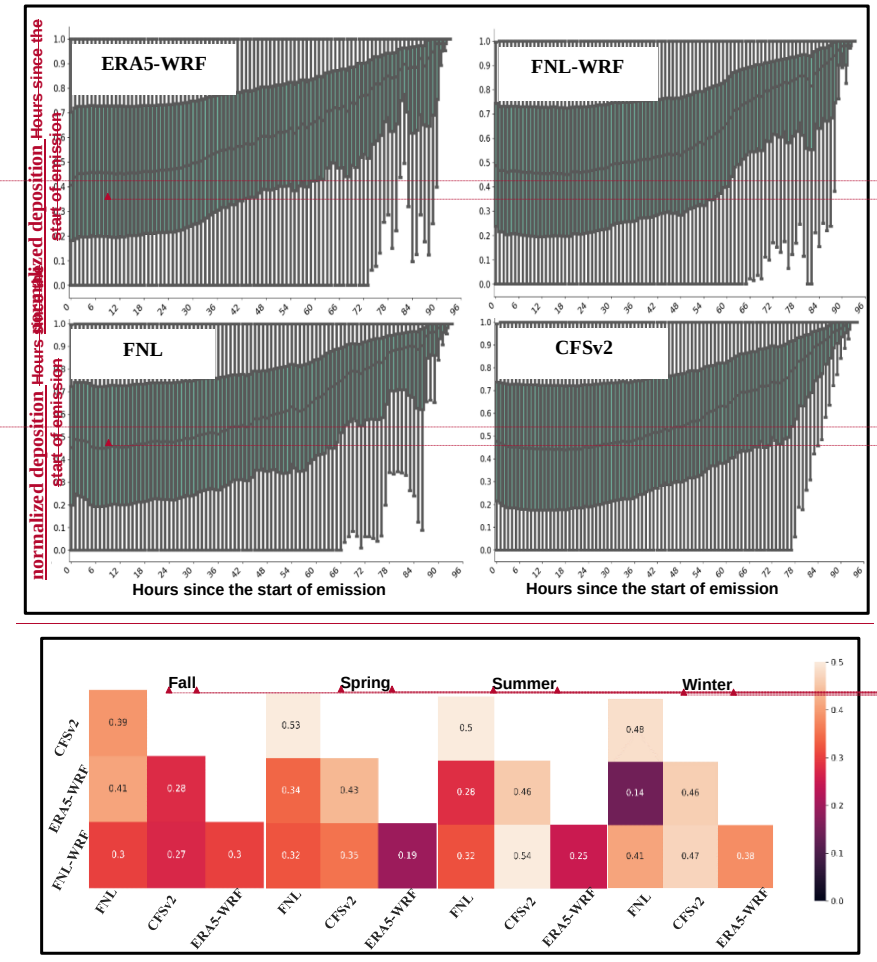

Figure 3 the seasonal maximum normalized difference of smooth density estimates of air parcel ages.

Due to the relatively long half-life of ^{137}Cs, its deposition rate in the affected areas is of great importance. ~~Figure 3 shows the relationship between the age compositions of air parcels and the amount of ^{137}Cs deposition~~ To analyze the relationship between the age composition of air parcels and the amount of ^{137}Cs deposition, the deposition values cumulatively summed

Formatted: Font: Bold, Complex Script Font: Bold
Formatted: Font: Bold, Complex Script Font: Bold
Formatted: Font: Bold, Complex Script Font: Bold
Formatted: Font: Bold, Complex Script Font: Bold
Formatted: Font: 8 pt, Complex Script Font: 8 pt
Formatted: Font: 6 pt, Complex Script Font: 6 pt
Formatted: Font: 8 pt, Complex Script Font: 8 pt
Formatted: Font: 6 pt, Complex Script Font: 6 pt
Formatted: Font: 8 pt, Complex Script Font: 8 pt
Formatted: Font: 6 pt, Complex Script Font: 6 pt
Formatted: Font: 8 pt, Complex Script Font: 8 pt
Formatted: Font: 6 pt, Complex Script Font: 6 pt

through time steps (j) and age spectra (i) are normalized to the total amount of ^{137}Cs deposition simulated at each grid cell (k) at the end of each simulation run (l)~~in winter when both dry and wet deposition occur in the study area~~.

$$^{137}Cs_{klta_{norm_depso}} = \begin{cases} \frac{\sum_{i=1}^{a} {}^{137}Cs_{klij}}{\sum_{j=1}^{96}\sum_{i=1}^{96} {}^{137}Cs_{klij}} & if\ j = 1 \\ \frac{\sum_{j=1}^{t-1}\sum_{i=1}^{96} {}^{137}Cs_{klij} + \sum_{i=1}^{a} {}^{137}Cs_{klij}}{\sum_{j=1}^{96}\sum_{i=1}^{96} {}^{137}Cs_{klij}} & if\ j > 1 \end{cases} \quad (9)$$

Figure 4 shows the normalized deposition amounts ($^{137}Cs_{klta_{norm_depso}}$) in winter when both dry and wet deposition occur in the study area. We found very similar results in other seasons (Fig. S5).

As expected, the values of the ^{137}Cs deposition increase cumulatively with the time after the accident. ~~and~~ All members simulated a similar pattern (median) in which around eighty percent of the deposition (the median of normalized deposition > 0.8) happens within 80 hours after the assumed accident. However, there is considerable variability in the spatial pattern of deposition. Given that the figure shows the amount of deposition across the whole study area, the decrease in the levels of accumulated deposition at the end of the simulation period pertains to the areas that are far from the source. However, in all parts of the region, the deposition is close to 100% approaching the end of the 96-hour simulation period. This can also be seen in Figure S6 where most of the particles inducing all intensities of ^{137}Cs deposition peak around 20 hours and a quite small number of air parcels are aged above 80 hours.

Formatted: Normal, Centered, Line spacing: single

Formatted: Font: Complex Script Font: +Headings (Times New Roman)

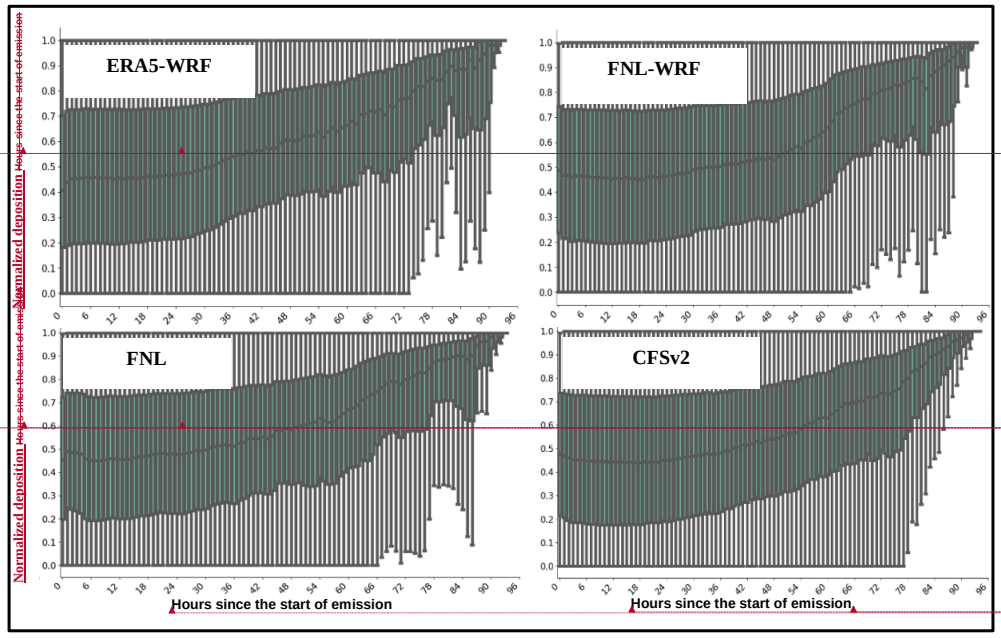

300

Figure 4~~3~~ the ~~maximum~~ total amount of each four-day simulation period at each grid cell ~~in winter~~. This plot (S5) shows simulations in winter (other seasons). ~~T~~he x-axis shows the age of Lagrangian particles and the y-axis is the normalized deposition. Error bars show the 25th and 75th percentiles (the lower and upper quartiles) and the range of normalized deposition (the upper and lower extremes) within the study area. ~~To prepare this plot, the deposition values for each time step are accumulated (through age spectra and time dimensions) and, then, are normalized to the maximum value of each four-day run at each grid cell.~~

3.2 Spatio-temporal distribution of radionuclides

In this section, we examine the seasonal and diurnal changes in the concentrations and deposition of radionuclides in the study area. To perform the analysis related to radionuclide concentrations, the thickness-weighted average of the simulations in the lowest four layers of the model between 5 to 100 meters has been used. Due to the high radioactivity of ^{131}I and the solubility and relatively long half-life of ^{137}Cs, in this part, we focus on ^{131}I concentrations and ^{137}Cs deposition. ~~Figures 4 and 5 show the seasonal median of the maximum ^{131}I concentrations ($^{131}I^{conc_seas_max}$) and of the maximum (total) ^{137}Cs deposition ($^{137}Cs^{depos_seas_max}$) within the study area. The maximum values are calculated through each four-day simulation period and,~~

Formatted: Font: 7 pt, Complex Script Font: 7 pt
Formatted: Font: 7 pt, Bold, Complex Script Font: 7 pt, B
Formatted: Font: 5 pt, Complex Script Font: 5 pt
Formatted: Font: 5 pt, Bold, Complex Script Font: 5 pt, B
Formatted: Font: 7 pt, Complex Script Font: 7 pt
Formatted: Font: 7 pt, Bold, Complex Script Font: 7 pt, B
Formatted: Font: 5 pt, Complex Script Font: 5 pt
Formatted: Font: 5 pt, Bold, Complex Script Font: 5 pt, B
Formatted: Font: 7 pt, Complex Script Font: 7 pt
Formatted: Font: 8 pt, Complex Script Font: 8 pt
Formatted: Font: 7 pt, Complex Script Font: 7 pt
Formatted: Font: 9 pt, Not Italic, Font color: Auto, Compl Script Font: 9 pt, Not Italic
Formatted: Tab stops: 4", Left

then, medians are found within the respective season. To identify the highest possible level of pollution at each point, regardless of its frequency, local maxima are calculated only from non-zero intensities. Using conversion factors fromthe model proposed by WHO (2012) for internal dose from inhalation Spiegelberg-Planer (2013), (WHO, 2012), $^{131}I_{conc_seas_max}$intg_conc_seas (in a unit of Bq m^{-3}) are is converted to tthe maximum hourly doses from inhalation he effective dose from inhalation of ^{131}I (in a unit of μSvμSv). The model inputs are specified for three age groups of 1-year-old infants, 10-year-old children, and adults (11 years old and up). Considering that about 90% of Qatar's population is in the adult age group (UNStats, 2020), the inhalation doses computed for this age group are discussed here (Fig. 5) and those for two others are available in the supplement (Figures S7 and S8). Results show that CFSv2 and FNL simulated the lowest and highest levels (above 150 μSv) of inhalation doses in all seasons in most parts of study area than the other members (note varying color scales between members in both Figures 4 and 5). While The other FLEXPART run, CFSv2, simulatedions are consistentlymuch lower levels of less than 200 μSvinhalation doses in all seasons, except in winter, FNL and two dynamically downscaled members simulated doses up to more than 1000 and 600 μSv. In other words, the forecast member of the ensemble has underpredicted ^{131}I doses by a factor of about 3 to 5 compared to (re)analysis members in severely polluted areas. Considering thatthe fact that FNL and CFSv2 are executed using the same simulation code, the remarkable difference between the resulting $^{131}I_{conc_seas_max}$intg_conc_seas and, subsequently, inhalation doses can be attributed to the difference in meteorological inputs. Figure S97 shows the seasonal median of planetary boundary layer height (PBLH) estimated based on CFSv2 (top row) and FNL (bottom row) meteorological inputs. CFSv2-based PBLH is found to be 3 to 5 times higher over emission point in UAE and, with less intensity, within the study area than FNL-based PBLH. The obvious consequence of elevated PBLH is the dilution of pollutants near the surface. In addition, the poorer spatial resolution of CFSv2 inputs caused the faulty separation of land and sea boundary layer process along the coastlines of Qatar. This also may lead to the suboptimal modeling of particle dispersion across the study area, especially along the coastlines. The inter-seasonal comparison of simulations in the south/southeast of Qatar shows a considerable increase (decrease) in inhalation doses during the cold period (warm period) of the year. It can be partly due to Ththee lower (higher) PBLH in the cold (warm) period of the year coincides with seasonsescalated (downgraded) $^{131}I_{conc_seas_max}$ by a factor of up to 3 to 5 in the cold period (warm period) in the south/southeast of Qatar. In other words, southern Qatar is the first area to be affected by dense ^{131}I clouds in the event of a nuclear accident, especially in the cold period of the year. FNL simulated a dense ^{131}I cloud in the center of Qatar in the summer that is due to an exceptional transport of radionuclides to Qatar in the summer of 2019, discussed later. This unusual pattern in summer, and even prevalent spatial patterns in other seasons, may change with the increasing length of the study period. Inhalation doses simulated by three reanalysis members in the southeast of Qatar are relatively high comparable compared to equivalent doses modeled by Christoudias and Lelieveld (2013) for areas adjacent to the Fukushima accident. Using conversion factors from (Spiegelberg-Planer, 2013), Tthey reported the cumulative inhalation of 100 and 500 μSv doses higher than 100 to 200 μSv from a total of ^{131}I, ^{134}Cs, and ^{137}Cs concentrations in around three months (between March 11 and May 31, 2011). We note that one should not expect our results to reproduce the simulations of the Fukushima NPP accident. In this study, we primarily aim to determine the relative risk by

Formatted: Font: (Default) Times New Roman, 10 pt, Not Bold, Font color: Auto, Complex Script Font: Times New Roman, 12 pt, Not Bold

Formatted: Font color: Auto, Pattern: Clear

Formatted: Font: (Default) Times New Roman, 10 pt, Font color: Auto, Complex Script Font: Times New Roman, 12 pt

Formatted: Font: (Default) Times New Roman, Font color: Auto, Complex Script Font: Times New Roman, 12 pt

Formatted: Font: (Default) Times New Roman, Font color: Auto, Complex Script Font: Times New Roman, 12 pt

Formatted: Default Paragraph Font, Font: (Default) Times New Roman, 10 pt, Not Bold, Font color: Auto, Complex Script Font: Times New Roman, 12 pt, Not Bold, Pattern: Clear

Formatted: Default Paragraph Font, Font: (Default) Times New Roman, 10 pt, Not Bold, Font color: Auto, Complex Script Font: Times New Roman, 12 pt, Not Bold, Pattern: Clear

highlighting variations in the spatio-temporal distribution of radionuclides in the study area due to differences in the diurnal and seasonal atmospheric processes and modeling conditions.~~Consequently, we have not sought to use the temporal and vertical profiles of radionuclide releases similar to those used for the modeling of Fukushima accident~~ C ~~C~~ompared to the outputs of FNL and FNL-WRF, the significant similarity of FNL-WRF and ERA5-WRF simulations suggests the downscaling of inputs and the application of the same (different) simulation codes can profoundly affect FLEXPART modelling. For example, the simulations of FNL in southern Qatar in ~~autumn~~ fall are more than twice that of FNL-WRF (more details in the subsection 3.3)~~WRF-FNL~~. In order to investigate the impact of particle release time on the extreme concentrations and deposition rate of the studied radioactive materials, the seasonal median of the particle release time simultaneous with the maximum concentration of ^{131}I and the completion of ^{137}Cs deposition are shown in Figures 5 and 6 with contours (in the unit of hour). To identify the highest possible level of pollution at each point, regardless of its frequency, local maxima are calculated only from non-zero intensities. The ~~examination of the particle release time (shown by contours) shows~~results show that the highest ^{131}I concentrations ~~^{131}I$_{conc_seas_max}$ i~~in most parts of the study area is caused by particles released between 5 a.m. and 12 p.m.. ~~-~~As mentioned before, it seems that the intensification of the thermal gradient between the land and sea at this time of day and the strengthened onshore winds increase the transfer of freshly released air parcels carrying concentrated ^{131}I clouds inland to the south of the study area. Figure 6~~5~~ shows ^{137}Cs$_{depos_seas_max}$~~tot_depos_seas~~ simulated by four ensemble members. According to the definition by the International Atomic Energy Agency (IAEA, 2009) any area covered with radioactive substances which emit beta particles and gamma rays, like ^{131}I and ^{137}C, in quantities above 40 kBqm−2 is considered to be contaminated. Accordingly, ~~-~~ all members have simulated high levels of contamination for a significant portion of the study area in the cold period of the ~~-~~year. For example, FNL simulations of ^{137}Cs$_{depos_seas_max}$~~tot_depos_seas~~ in winter and ~~autumn~~fall ~~-~~are above 40 kBqm−2 (and even above 90 kBqm−2) in entire southern Qatar. ~~-~~ Contrary to ^{131}I$_{conc_seas_max}$~~intg_conc_seas~~, CFSv2 yielded comparable and even higher ^{137}Cs$_{depos_seas_max}$~~tot_depos_seas~~ to other members in winter when the entire Qatar is subject to ^{137}Cs$_{depos_seas_max}$~~tot_depos_seas~~ of more than ~~100~~ 90 kBqm−2. However, in other seasons, CFSv2 simulations fall below 40 kBqm−2 in most areas. In the simulations of ERA5- and FNL-WRF, ^{137}Cs$_{depos_seas_max}$~~tot_depos_seas~~ levels above 40 kBqm−2 cover almost the entire ~~–~~ Qatar in winter whereas they are confined to the southern half in ~~autumn~~fall. The ^{137}Cs$_{depos_seas_max}$~~tot_depos_seas~~ magnitudes in the warm period of the year (except in the simulations of FNL in summer) are mostly either close to or below the threshold. The higher ^{137}Cs$_{depos_seas_max}$~~tot_depos_seas~~ in the cold period of the year, especially in winter, can be largely attributed to the seasonal increase in the transport of ^{137}Cs by northward winds, discussed later, and to the increased contribution of wet deposition. According to Figure S2, the wet deposition of ^{137}Cs in CFSv2 simulations is greater than that of other members, which can well explain the higher CFSv2 ^{137}Cs$_{depos_seas_max}$~~tot_depos_seas~~ in winter. The above results indicate that if a nuclear accident happens in the cold period of the year, especially in winter, the magnitudes of extreme ^{131}I concentrations and total ^{137}Cs deposition in the south of Qatar can be up to 3 times stronger than in the warm seasons. In Figure 6~~5~~, ^{137}Cs$_{depos_seas_max}$~~tot_depos_seas~~ mainly coincides with the contours of particle release time between 10 a.m. and 2 p.m. when the boundary layer is expanding. The analysis of age spectra in subsection 3.1 disclosed the greater frequency of long-lived air

parcels in FNL simulations. To further examine these results, the spatial distribution of air parcel ages overlying the full-year median of the ~~maximum~~ 96-hour integrated ^{131}I concentrations (inhalation does for the adult age group) and of the ~~maximum (total)~~total of ^{137}Cs deposition is shown in Figures 7~~6~~-A and -B, respectively. As expected, the age of Lagrangian particles is decreasing southward with the decreasing distance from the source. In Figure 7~~6~~-A, we see that all ensemble members simulated the age contours of less than 20 hours along with high levels of ^{131}I at the south-eastern corner of the study area. The longer-lived particles (above 37 to 40 hours) were found in the north of Qatar. The observation of longer-lived air parcels and expanded dense ^{131}I clouds in the ~~center~~ north of Qatar in FNL simulations indicate a higher frequency of air parcels reaching further receptors from the source~~slower air parcel transport~~ and the greater expansion of radionuclides in the northern fringe of study area~~to areas further from the source~~. ~~Therefore, these two transport characteristics seem~~ This (not a decrease in transport speed to the same receptors) seems to cause the abundance of longer-lived particles in FNL simulations compared to other members. ~~The residence time of Lagrangian particles, as the third factor, is not investigated in the present study because it is not the standard output of forward FLEXPART runs.~~ According to Figure 7~~6~~-B, FNL simulated the fastest end to the total ^{137}Cs deposition in southern Qatar (about ~~40~~ 35 hours after the accident) whereas air parcel ages corresponding to the deposition completion in the north of Qatar are above about 60 hours in all members. In other words, FNL produced the biggest difference (around 20-25 hours) between the particle ages simultaneous with the completion of ^{137}Cs deposition in the north and south of Qatar compared to that of other members (around 10-15 hours).

Formatted: English (United Kingdom)

Formatted: Font: (Default) +Headings (Times New Roma 10 pt, Not Bold, Complex Script Font: +Headings CS (Time New Roman), 12 pt, Not Bold, (Complex) Persian (Iran), English (United Kingdom)

Formatted: English (United Kingdom)

Formatted: Font: (Default) Times New Roman, Complex Script Font: Times New Roman, (Complex) Arabic (Saudi Arabia), English (United Kingdom)

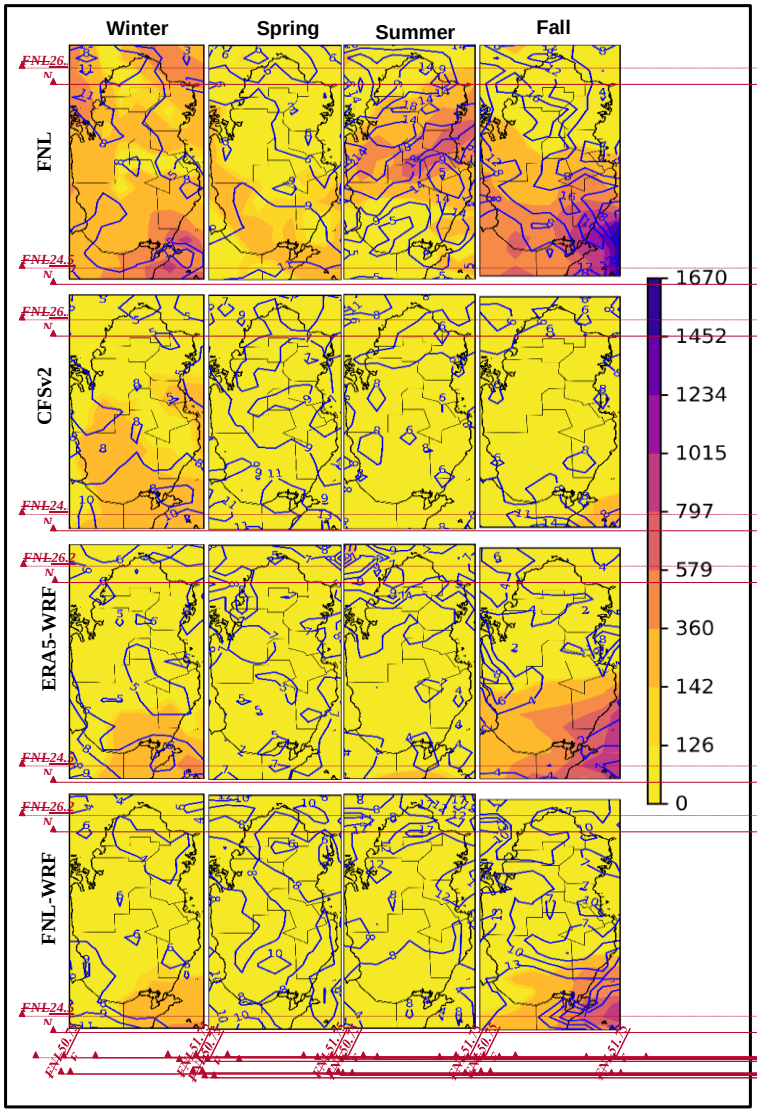

Formatted
Formatted
Formatted
Formatted
Formatted
Formatted
Formatted
Formatted
Formatted
Formatted
Formatted
Formatted
Formatted

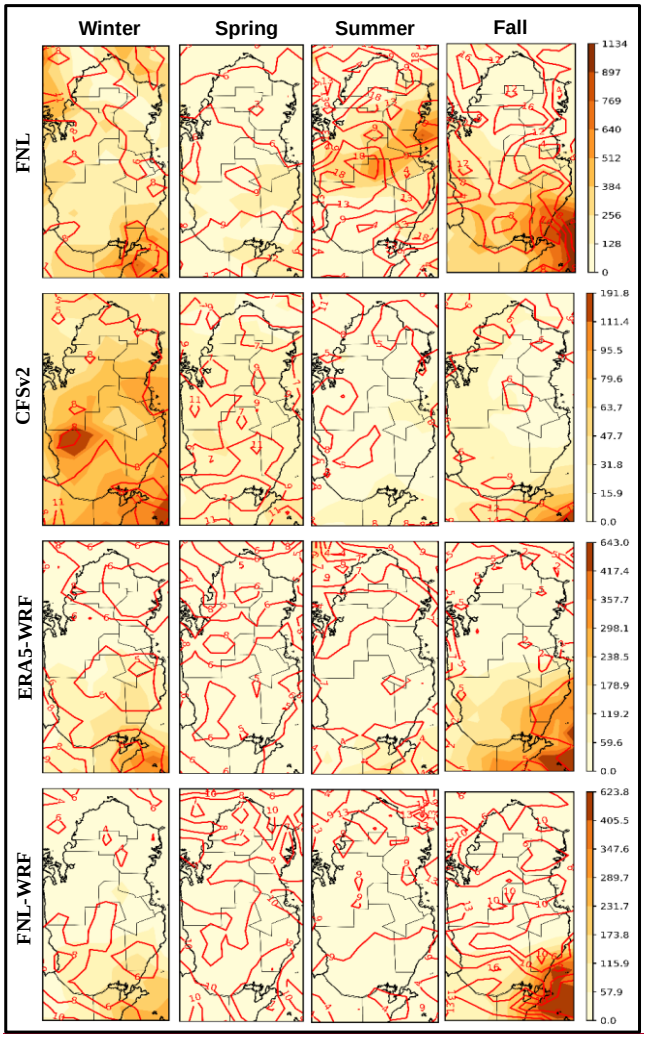

Figure 54 Color scale shows the seasonal median of ~~maximum~~ the 96-hour integrated ^{131}I concentrations (^{131}I~~conc_seas_maxintg_conc_seas~~), converted to the effective doses from ~~maximum hourly doses from~~ inhalation ~~s~~ (~~μSv~~μSv) for the adult age group. Contour lines (in the unit of hour) are the seasonal median of release time of Lagrangian particles simultaneous with the maximum ^{131}I concentrations of each 96-hour run.

~~FNL~~26.2

Formatted: Font: Bold, Complex Script Font: Bold

Formatted: Font: (Default) +Headings CS (Times New Roman), 9 pt, Bold, Font color: Auto, Complex Script Font: +Headings CS (Times New Roman), 9 pt, Bold, (Complex) Persian (Iran), English (United States)

Formatted: Font: (Default) +Headings CS (Times New Roman), 9 pt, Bold, Complex Script Font: +Headings CS (Times New Roman), 9 pt, Bold, (Complex) Persian (Iran), English (United States)

Formatted: Font: 7 pt, Italic, Complex Script Font: 7 pt, Italic

Formatted: Font: 6 pt, Italic, Complex Script Font: 6 pt, Italic

Formatted: Font: 7 pt, Italic, Complex Script Font: 7 pt, Italic

Formatted: Font: 6 pt, Italic, Complex Script Font: 6 pt, Italic

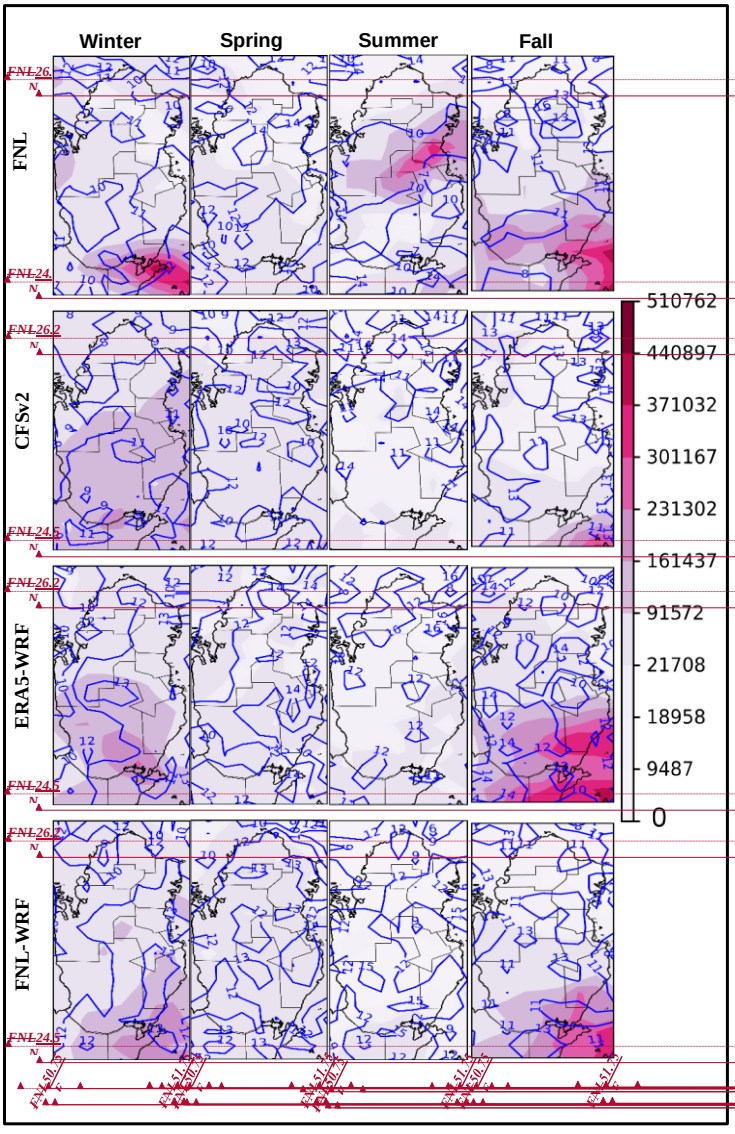

Formatted
Formatted
Formatted
Formatted
Formatted
Formatted
Formatted
Formatted
Formatted
Formatted
Formatted
Formatted
Formatted
Formatted

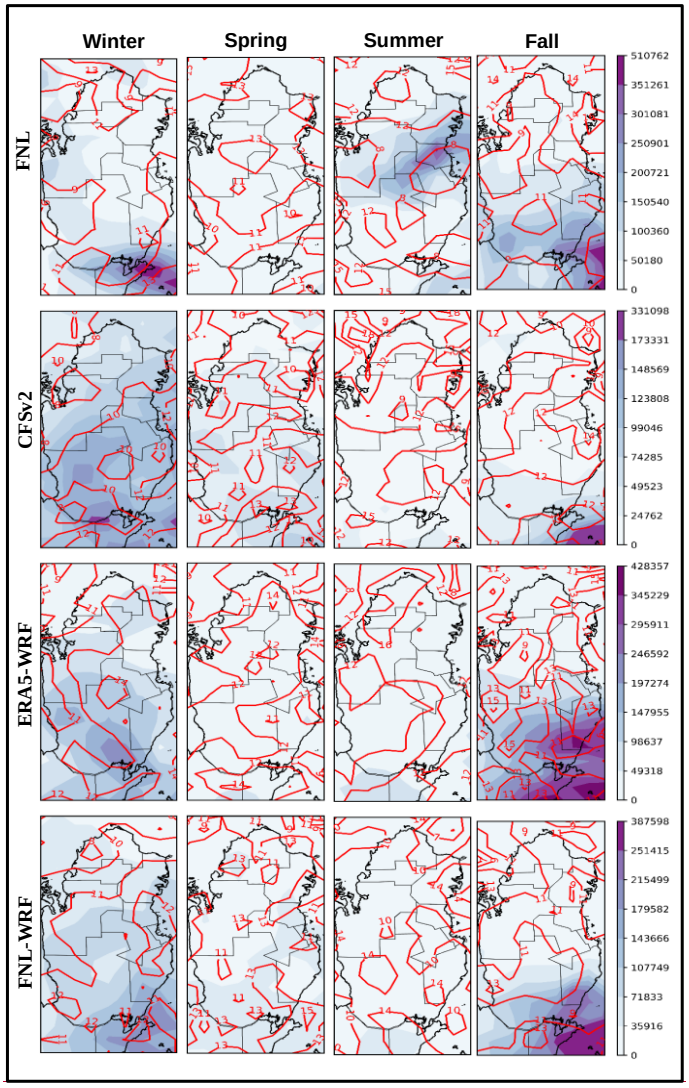

Figure 65 Same as 54, but for the seasonal median of ^{137}Cs deposition ($^{137}Cs^{depos_seas_max}$~~tot_depos_seas~~) in the unit of Bqm^{-2}.

405

Because of the high importance of the population being exposed to air pollution radionuclides, ^{131}I~~conc_seas_max~~intg_conc_seas, converted to the maximum hourly doses from inhalation, and ^{137}Cs~~depos_seas_max~~tot_depos_seas are analyzed against the population density of Qatar (Fig. ~~8~~7). The spatial distribution of the population shows that the desert areas of southern and southeastern Qatar, as the domain entry of radionuclides in the region, host a small number of people or are nearly uninhabited (Fig. ~~8~~7-A). Figures ~~8~~7. —B and C show that the extremely high levels of inhalation doses (higher than 200 μSv) and of ^{137}Cs~~depos_seas_max~~tot_depos_seas (higher than 100 kBqm−2) occurred mostly in areas with a population density of fewer than five people per arc-second. The populated areas (with a density of more than 15 people per arc-second) exhibit lower expected inhalation doses and ^{137}Cs^{tot_depos_seas} less than 200 μSv and 100 kBqm−2~~thresholds~~. The highest inhalation doses are often found in FNL simulations, in ~~autumn~~fall –and winter, whereas the lowest doses are simulated by CFSv2. Compared to ^{131}I~~conc_seas_max~~intg_conc_seas inhalation doses, there are no pronounced seasonal and inter-member differences in ^{137}Cs~~depos_seas_max~~tot_depos_seas at different population levels.

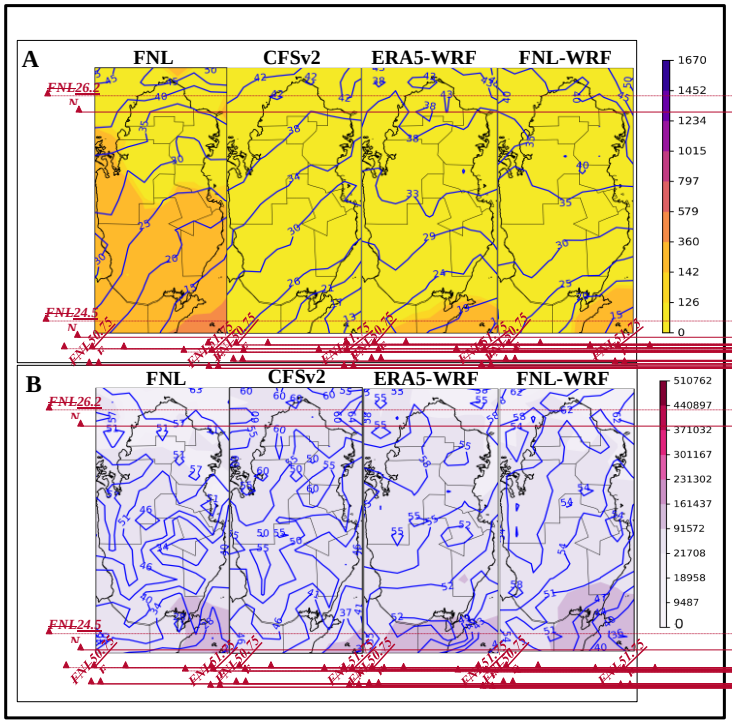

Formatted
Formatted
Formatted
Formatted
Formatted
Formatted
Formatted
Formatted
Formatted
Formatted
Formatted
Formatted
Formatted
Formatted
Formatted
Formatted
Formatted
Formatted
Formatted

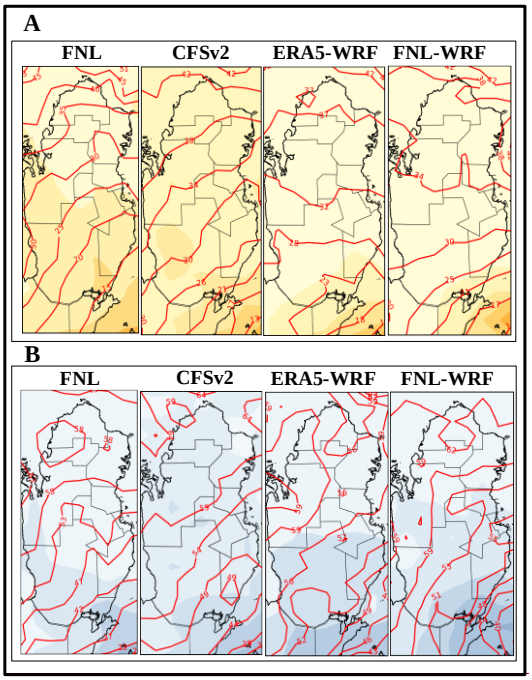

Figure 7~~6~~ A: the full-year median of ^{131}I ~~conc_seas_max~~intg_conc_seas), converted to maximum hourly doses from inhalations (μSv) for the adult age group, and B: the full-year median of ^{137}Cs deposition (^{137}Cs ~~depos_seas_max~~tot_depos_seas) in the unit of Bqm^{-2}. Contour lines are the full-year median of air parcel ages (hour) simultaneous with maximum ^{131}I ~~131I~~ concentrations and total ^{137}Cs ~~137Cs~~ deposition. ~~The colorbar of each subplot, representing each member, in the top~~

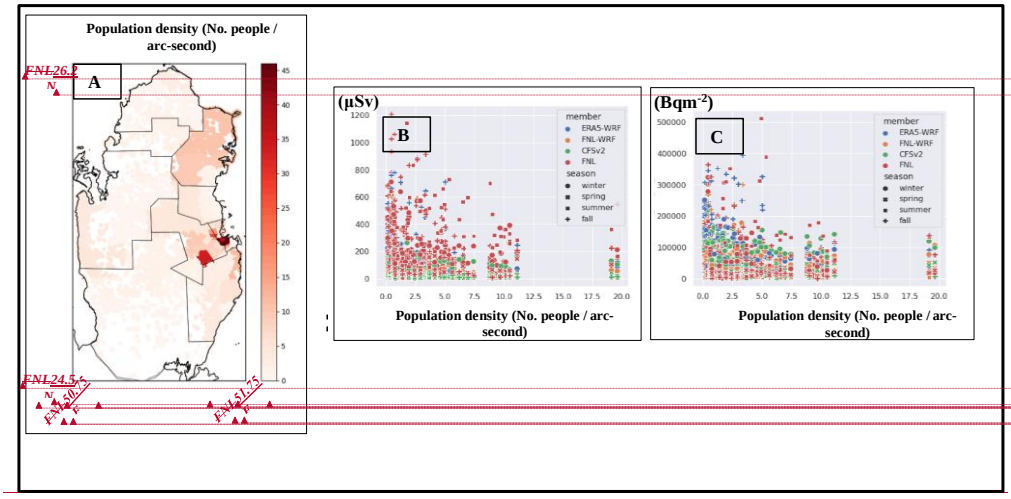

~~(bottom) row is the same as in Fig. 4 (Fig. 5), omitted here for space.~~

Formatted: Font: 7 pt, Italic, Complex Script Font: 7 pt, Italic

Formatted: Font: 6 pt, Italic, Complex Script Font: 6 pt, Italic

Formatted: Font: 7 pt, Italic, Complex Script Font: 7 pt, Italic

Formatted: Font: 6 pt, Italic, Complex Script Font: 6 pt, Italic

Formatted: Font: 7 pt, Italic, Complex Script Font: 7 pt, Italic

Formatted: Font: 7 pt, Complex Script Font: 7 pt

Formatted: Font: 7 pt, Italic, Complex Script Font: 7 pt, Italic

Formatted: Font: 7 pt, Italic, Complex Script Font: 7 pt, Italic

Formatted: Font: 7 pt, Complex Script Font: 7 pt

Formatted: Font: 7 pt, Italic, Complex Script Font: 7 pt, Italic

Formatted: Font: 7 pt, Complex Script Font: 7 pt

Formatted: Font: 6 pt, Italic, Complex Script Font: 6 pt, Italic

Formatted: Font: 7 pt, Complex Script Font: 7 pt

Formatted: Font: 6 pt, Italic, Complex Script Font: 6 pt, Italic

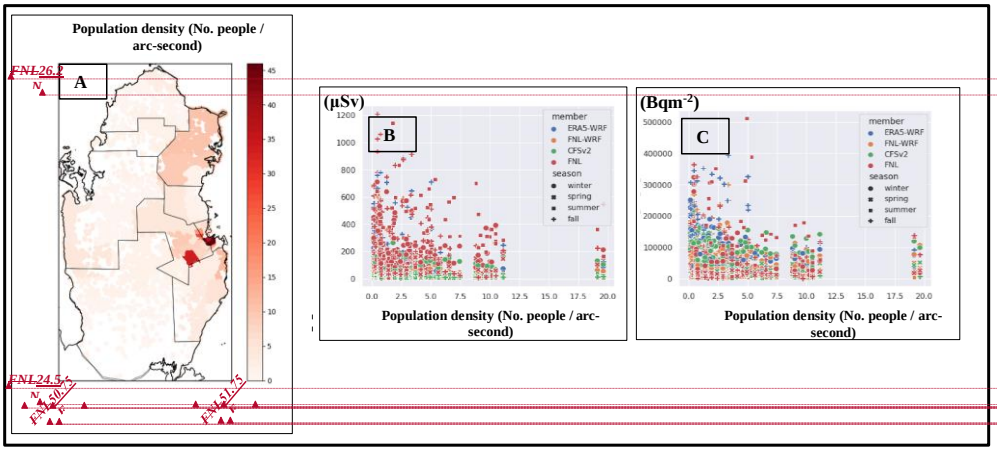

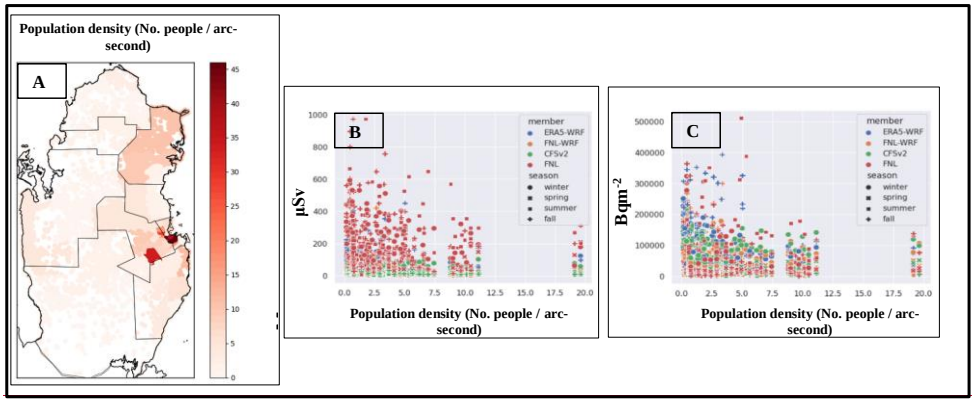

Figure ~~8~~7 the subplot A shows the gridded number of the population of Qatar at a resolution of one arc-second in 2020. The relationship between ^{131}I~~conc_seas_max~~intg_conc_seas, converted to maximum hourly doses from inhalation~~s~~ (~~μSv~~μSv), and ^{137}Cs~~depos_seas_max~~tot_depos_seas and Qatar's population densities are shown in B and C, respectively. Markers' shapes and colors represent seasons and ensemble members.

In addition to the ~~magnitude of~~magnitude of the radioactive materials transported, the temporal distribution of extreme events in the affected area is of importance in preparedness programs. Figure ~~9~~8-A shows the frequency of occurrences (FoO) of ^{131}I column densities above the 66th percentile. In all members, more than half of the events in the east, with a high population density, and north of Qatar occurred in winter. Other parts of Qatar also see a large FoO (greater than 30% in FNL-WRF to 50% in FNL) in winter. While the springtime FoO of high ^{131}I varies between 15 and 30%, the lowest FoO is observed in the

Formatted: Font: 7 pt, Italic, Complex Script Font: 7 pt, Italic

Formatted: Font: 6 pt, Italic, Complex Script Font: 6 pt, Italic

Formatted: Font: 7 pt, Italic, Complex Script Font: 7 pt, Italic

Formatted: Font: 6 pt, Italic, Complex Script Font: 6 pt, Italic

Formatted: Font: 7 pt, Italic, Complex Script Font: 7 pt, Italic

Formatted: Font: 7 pt, Complex Script Font: 7 pt

Formatted: Font: 7 pt, Italic, Complex Script Font: 7 pt, Italic

Formatted: Font: 7 pt, Italic, Complex Script Font: 7 pt, Italic

Formatted: Font: 7 pt, Complex Script Font: 7 pt

Formatted: Font: 7 pt, Italic, Complex Script Font: 7 pt, Italic

Formatted: Font: 7 pt, Complex Script Font: 7 pt

Formatted: Font: 6 pt, Italic, Complex Script Font: 6 pt, Italic

Formatted: Font: 7 pt, Complex Script Font: 7 pt

Formatted: Font: 6 pt, Italic, Complex Script Font: 6 pt, Italic

summer when less than 15% of extreme events have reached receptors in Qatar. The seasonal FoO of ^{137}Cs column densities (S10~~8~~) also shows almost identical results. The panel at the top in Figure 9~~8~~-B shows a case in which ERA5-WRF simulated the north-westward movement of ^{131}I concentrations (Bq/m3) on January 14 at noon. We observe a similar pattern in a large number of events during which high levels of radionuclides are transported to Qatar. This synoptic pattern seems to be due to the juxtaposition of low and high-pressure cells located in the west and east of the region. The resulting pressure gradient has caused the formation of strong south/southeast winds between two cyclonic and anti-cyclonic cells that move the dense ^{131}I clouds to the study area. This pattern occurs mainly in the late winter-early spring period simultaneous with the southward movement of westerlies and the eastward movement of the Saudi Arabian subtropical high pressure (De Vries et al., 2016). The panel at the bottom in Figure 9~~8~~-B shows the summertime average of ERA5-WRF ^{131}I concentrations (Bq/m3) and of near-surface atmospheric circulation. The seasonal pattern found here illustrates well the main reason for the scarcity of extreme events observed in summer in the study area. In this pattern, northwest-southeast winds, known as Shamal winds (Yu et al., 2016), caused simulated radionuclides to move away from the study area. Therefore, one may assume that the occurrence of a nuclear accident and the resulting release of radionuclides in the cold period of the year pose a higher contamination risk to the population in Qatar.

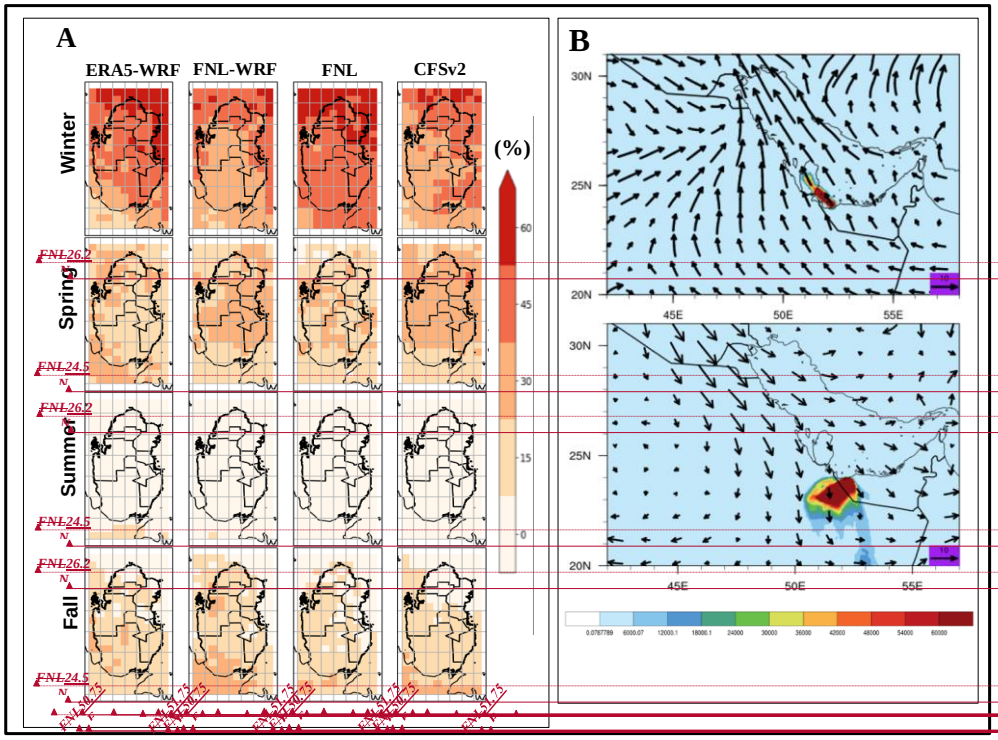

Concerning the sensitivity analysis of FLEXPART-WRF simulations to the turbulence scheme of choice, the use of STM overall reduces the column densities aggregated over each 96-hour simulation period (96-hour integrated column densities). As shown in Figure 10-A, the median of simulated column densities of ^{131}I is more than doubled in GTM-based simulations in the fall. There is no comparable change in other seasons that is reflected in a minute increase in the full-year distribution of GTM-based simulations. In contrast, we see a tangible increase in extremely high levels of STM-based ^{137}Cs deposition simulations in almost all seasons (Fig. 10-B). The upper quartile of ^{137}Cs deposition with STM in winter is around 25% higher than those simulations with GTM in the same period. This is largely found across the year leading to an annual increase of around 20% in the upper quartiles of STM-based simulations of ^{137}Cs deposition. The implementation of STM in FNL-WRF has had a similar impact on radionuclide simulations (shown in ~~S9~~S11). The increase in high ^{137}Cs deposition and the decline in the moderate levels of ^{131}I column densities (mainly in fall) after the application of STM, in both sensitivity runs, can be

Formatted
Formatted
Formatted
Formatted
Formatted
Formatted
Formatted
Formatted
Formatted
Formatted
Formatted

interpreted as the increase of deposition in areas closer to the emission point and the equivalent decline in the transport of radionuclides to remote areas, respectively.

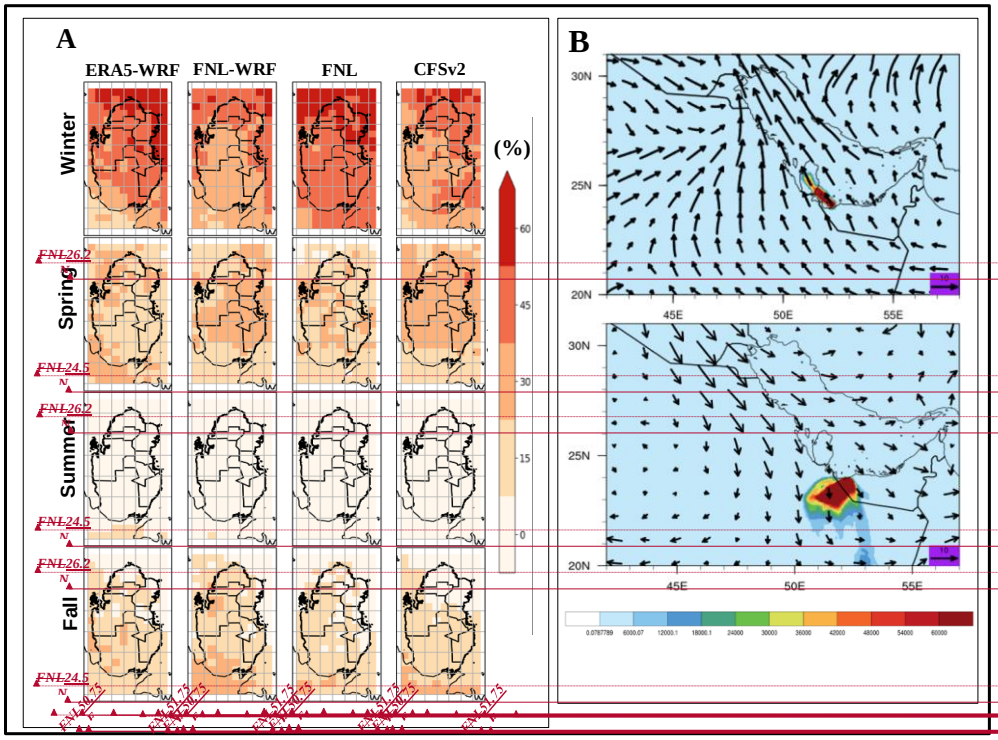

Figure 98 A: The frequency of occurrence (%) of ^{131}I column densities above the respective 66th percentile. B: ERA5-WRF ^{131}I column density (Bq m-3) on January 14, 2019, at noon (top) and the summertime average of ^{131}I column density (bottom). Overlaying vectors show wind streams at 150 m agl. To represent atmospheric circulations during the release of radionuclides, wind data at 12 p.m. on the first day of the four-day simulation period was used.

Formatted
Formatted
Formatted
Formatted
Formatted
Formatted
Formatted
Formatted
Formatted
Formatted
Formatted
Formatted
Formatted

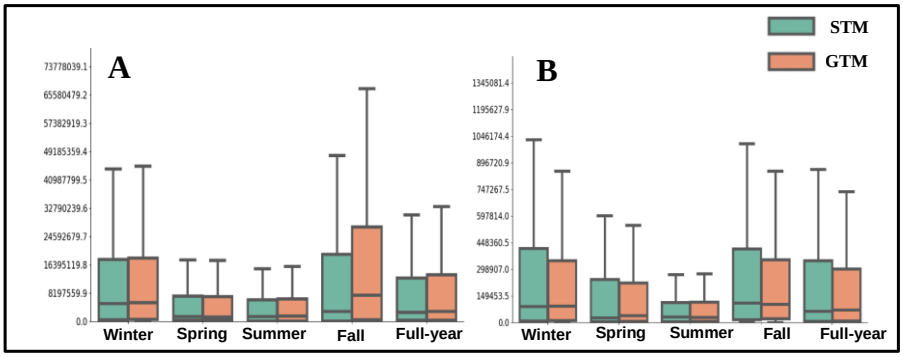

Figure 10 Panels A and B show the 96-hour integrated simulations of column densities of ^{131}I (Bq/m2) and total deposition of ^{137}Cs (Bq/m2) from ERA5-WRF with STM (green, sensitivity run) and GTM (brown, control run), respectively. The same outputs for FNL-WRF are shown in S9S11.

3.3 Inter-comparison of FLEXPART and FLEXPART-WRF runs (effect of downscaling)

Aside from the fact that radionuclides released from a nuclear accident are rarely monitored (Evangeliou et al., 2017), since we are dealing with a hypothetical accident in this study, the simulations from the three (re)analysis members are assumed to be a better approximation to actual conditions than that of CFSv2 (Leadbetter et al., 2022). The evaluation statistical metrics used here are recommended by Maurer et al. (2018) who sought the best transport model for the simulation of Xe-133 dispersion using measurements from the six International Monitoring System (IMS) stations. Besides other common evaluation metrics, they used the fractional bias (FB) and the fraction within a factor of 5 (F5). FB, in the range -2 and 2, is the bias of simulation means normalized by the sum of the two means and multiplied by 2. F5 is the fraction of simulations that is at most a factor larger (5) or smaller (0.2) than the reference values. The R-squared obtained between the 96-hour integrated simulations of ^{131}I column densities from CFSv2 and other members (the ~~bottom~~ first column from the right ~~row~~ in Figure 10~~10~~11) indicates that the CFSv2 simulations are well associated with those from (re)analysis members. The Pearson correlation coefficients between CFSv2 and (re)analysis simulations, equivalent to the square root of the coefficient of determination (r^2), range between 0.5 and 0.6. Maurer et al. (2018) found that the involved models produced an average correlation coefficient of 0.51 between Xe-133 simulations and observations. The highest correlation of CFSv2 was found with FNL followed by FNL-WRF. ~~The linear regression equations computed between simulations from CFSv2 and other members all have less than unity coefficients indicating that CFSv2 underpredicted ^{131}I column densities, especially compared to FNL.~~ The seasonal regression suggests that, mainly due to elevated PBLH (Fig. ~~S7~~S9), the simulations of CFSv2 are significantly lower than that of FNL in spring and that of FLEXPART-WRF members in summer. ~~The fractional bias (FB), in the range -2 and 2, is the bias of simulation means normalized by the sum of the two means and multiplied by 2. The fraction within a factor of 5 (F5) is the~~

~~fraction of simulations that is at most a factor larger (5) or smaller (0.2) than the reference values.~~ While CFSv2 simulations show (on average) trivial FB compared to FNL simulations, they are positively biased (~~-~~0.51 and ~~-~~0.58) compared to the simulations from FNL- and ERA5-WRF ~~(the negative sign of FB is due to the placement of the (re)analysis members in the x-axis)~~. In terms of FB5, 67.4% and 66.6% of CFSv2 simulations are respectively within the factor of 5 of FNL and FNL-WRF simulations while it is reduced to 56% in ~~-~~comparison against ERA5-WRF simulations. Taking into account the average FB of 0.33 and FB5 of 32% between simulations and observations reported by Maurer et al. (2018), it can be concluded that the association between CFSv2 and (re)analysis simulations falls within the expected range in radionuclide dispersion modeling. Unlike previous metrics, the RMSE between CFSv2 and FNL is higher than what was found between the former and other members. It is mainly because of the abundance of extremely high values in FNL simulations. CFSv2 simulations produced the lowest and highest NMSE, the normalized RMSE which is less sensitive to extreme values, against FNL (1.5) and ERA5-WRF (2.~~8~~) simulations, respectively. Among the (re)analysis members, the lowest correlation (0.61) is found between ERA5-WRF and FNL. Feeding downscaled FNL inputs into FLEXPART-WRF (FNL-WRF) increased the correlation of ERA5-WRF and FNL-WRF to 0.7. The highest correlation between all members was obtained between FNL and FNL-WRF (0.71) indicating that the downscaling of inputs in FNL-WRF did not have much effect on the association of their simulations. However, considering other metrics (FB=~~-~~0.07, FB5=79.3%, RMSE=~~75440~~14.6, and NMSE=1.~~2~~3), the closest simulations are produced by FNL-WRF and ERA5-WRF (rather than by FNL and FNL-WRF). This suggests that the downscaling of similar (FNL) and different (FNL and ERA-5) meteorological datasets increased and decreased the absolute differences between resulting simulations, respectively. The main diagonal of the evaluation matrix shows the relative distribution of simulations. All distributions here depicted the higher frequency of low ^{131}I column densities in spring than in other seasons (as also seen in Figure 2-A). The correlations computed between ^{137}Cs column densities in all members are very similar to those found for ^{131}I column densities ~~with the exception that the correlation between the CFSv2 and ERA5-WRF decreased from 0.7 to 0.64~~ (Fig. S1~~2~~0). ~~CFSv2 caused higher underpredictions compared to FNL- and ERA5-WRF in ^{137}Cs column density simulations, leading to the decrease of the respective linear coefficients from 0.9 and 0.77 to 0.64 and 0.53.~~ While the RMSEs have increased tangibly, FB and NMSE decreased up to zero and 1, r~~.2, r~~espectively, and FB5 increased up to 83%. This indicates that ^{137}Cs column density simulations from CFSv2 are less biased against (re)analysis members than ^{131}I simulations.

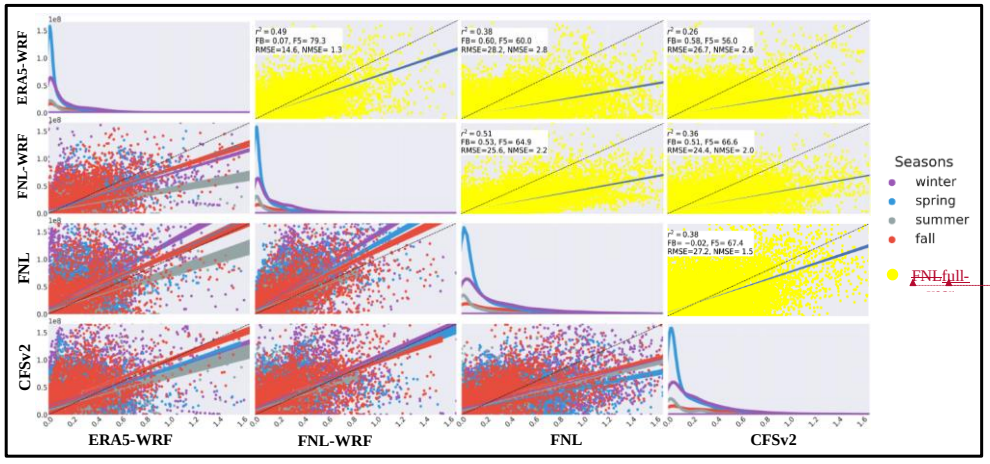

Figure 1110 The inter-comparison of the 96-hour integrated simulations of ^{131}I column densities (Bq/m2) from FLEXPART and FLEXPART-WRF runs. The reported model metrics, in the upper triangle of evaluation matrix plot, show the performance of members for all simulations over 2019 (full-year) at each grid point. Solid and dotted lines respectively show regression and identity lines. The seasonal regression lines are ~~shown~~ differentiated by colors in the lower triangle. ~~.~~ The density plot (unitless) in the main diagonal of the evaluation matrix shows the relative distribution of simulations.

The comparison of simulated ^{137}Cs deposition shows that ensemble members (both forecast and (re)analysis members) have simulated differently (Fig. S121). For example, CFSv2 yielded correlations of less than 0.22 compared with the three (re)analysis members. ~~The linear coefficients between CFSv2 and (re)analysis members are less than 0.1, which indicates much stronger underpredictions in CFSv2 deposition simulations than its column density simulations.~~ The other statistics not only emphasize the inconsistencies between CFSv2 and (re)analysis members but between (re)analysis members. Although there exists relatively higher consistency between the simulations of ^{131}I deposition (Fig. S132) than ^{137}Cs deposition, they are still far less correlated than the simulated column densities of both studied radioactive substances. Gudiksen et al. (1988) found errors in precipitation and the deposition formulation as two main sources of uncertainties in deposition modeling. Having compared meteorological fields from ERA-40 and ERA-Interim to force FLEXPART, Evangeliou et al. (2017) also found very large differences (around 55%) in the posterior source term of ^{137}Cs. It is attributed to differences in the precipitation fields of these two meteorological datasets that induced substantial differences in ^{137}Cs deposition (and subsequently in the estimated ^{137}Cs emissions). We also expect that part of the difference between ^{137}Cs deposition can be attributed to the recent updates in FLEXPART scavenging scheme, compared to the one used in FLEXPART-WRF.

Formatted: Font: Not Bold, Complex Script Font: Not Bold

Formatted: Font: Not Bold, Complex Script Font: Not Bold

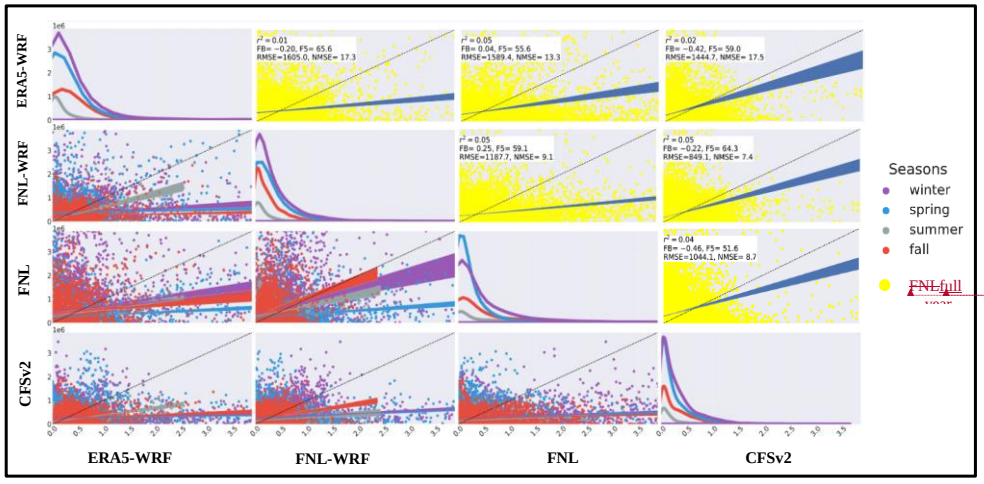

Figure 12~~10~~ Same as Figure ~~10~~ 11 but for ^{137}Cs deposition

Formatted: Font: Not Bold, Complex Script Font: Not Bold

Formatted: Font: Not Bold, Complex Script Font: Not Bold

Formatted: Font: (Default) +Headings CS (Times New Roman), 9 pt, Bold, Complex Script Font: 9 pt, Bold, Italic, (Complex) Persian (Iran)

Conclusion

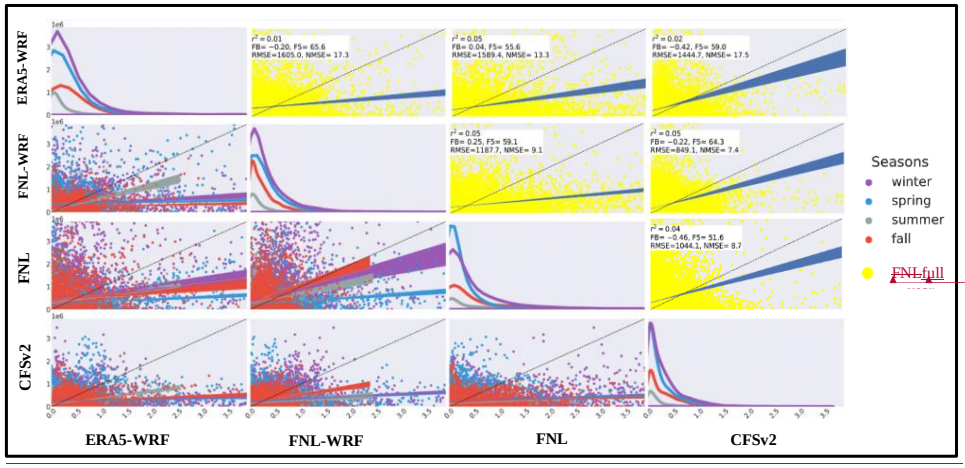

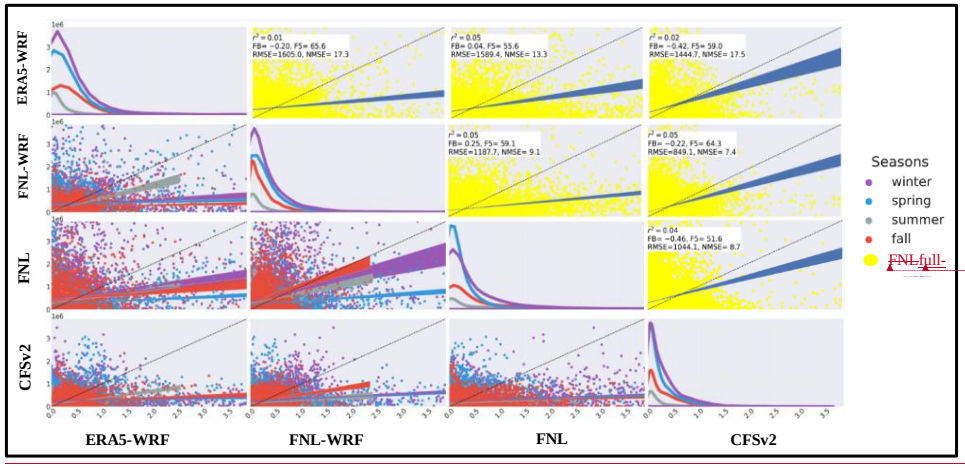

In this study, we examined the dispersion of radionuclides, including ^{131}I and ^{137}Cs, in the event of a nuclear accident at different seasons and times of the day. We have used the Lagrangian particle/air parcel dispersion model FLEXible PARTicle (FLEXPART) and FLEXPART coupled with the Weather Research and Forecasting model (FLEXPART-WRF). The studied radionuclides are assumed to be released within the first 24 hours of a four-day simulation period from an accident at the

Formatted: English (United States)

Formatted: Font: Not Bold, Complex Script Font: Not Bold

Formatted: Font: Not Bold, Complex Script Font: Not Bold

Formatted: Font: Not Bold, Complex Script Font: Not Bold

Formatted: Font: Not Bold, Complex Script Font: Not Bold

Barakah nuclear power plant (B-NPP) in the UAE. FLEXPART and FLEXPART-WRF were run iteratively 365 times (simulating each day of 2019) to produce hourly simulations through 96 hours after the accident at the spatial resolution of 10 km in 14 vertical levels from 5 to 5000 m agl. The source term was scaled to the maximum estimates of the radioactive materials from the Fukushima accident in 2011 (22 PBq (6.9 kg) of ^{137}Cs and 192 PBq (0.042 kg) of ^{131}I). In the course of examining the study question, we paid special attention to the differences in the simulations when using different meteorological inputs. We quantified meteorological uncertainties by producing an ensemble model with three (re)analysis members including Final Analysis (FNL) at native resolution, FNL and the ECMWF reanalysis 5th generation (ERA5) downscaled by WRF (FNL- and ERA5-WRF), and one forecast member which is forced by the NCEP climate forecast system version 2 (CFSv2). This ensemble provided the basis for comparing the output of the forecast member (CFSv2) against three other (re)analysis members. The simulations of FNL and CFSv2 were compared against that of FNL-WRF and ERA5-WRF to find the effect of downscaling and using different model simulation codes (FLEXPART vs. FLEXPART-WRF) on FLEXPART dispersion modeling. The simulations of all four members were also examined concerning the population density of Qatar to study pollution risks for local human communities in case of a nuclear accident in the region. We also studied the sensitivity of ERA5- and FNL-WRF simulations to the turbulence scheme used under convective conditions. The results of this study can be summarized in three main points:

1- **The transport of radionuclides:** to analyze the time interval between emission and reception of radionuclides, we used the age composition of radionuclide plumes. The results show that the transport characteristics of ^{131}I and ^{137}Cs did not significantly affect their movement from B-NPP to Qatar, the study area, which was attributed to the lack of heavy precipitation in the study area. Regardless of the time of release, the analysis of air parcel age spectra indicates that dense radionuclide clouds enter the south study area about 10 to 20 hours after the emission. A significant portion of emitted ^{131}I is transported to the furthest parts of the study area up to 80 hours after the accident. All members also simulated that a big portion of ^{137}Cs deposition occurs within 75 to 80 hours after the emission. The age distributions of Lagrangian particles in spring follow a bimodal distribution indicating the distant transport of radionuclides in this season. Results also show that the number of long-lived air parcels was higher when released between 12 p.m. and 6 p.m. This may indicate the impact of the planetary boundary layer height on the range of affected areas. ~~Compared to other members, the relatively lower spatial resolution of meteorological inputs caused the distribution of air parcel ages from CFSv2 to represent an average of other members' age distributions. In addition, t~~The lower temporal resolution of CFSv2 inputs and, consequently, abrupt changes in the diurnal variation of boundary layer height caused the infrequency of long-lived particles after sunset in the resulting simulations. The age distributions produced by FNL-WRF and ERA5-WRF were found to be more similar, compared to the one from FNL, due to the downscaling of inputs and the use of a common simulation code. The larger contribution of long-lived particles in FNL simulations was distinctively found in all seasons. We attributed it to the ~~slower and/or~~ more distant transport of air parcels from the emission point in FNL simulations, compared to other members.

2- **The distribution of extremely high concentrations and deposition of radionuclides:** we investigated the seasonal median of the ~~maximum~~ 96-hour integrated~~of~~ ^{131}I concentrations (^{131}I~~conc_seas_max~~intg_conc_seas), which is converted to the maximum hourly doses from inhalation, and of the total ^{137}Cs deposition (^{137}Cs~~depos_seas_max~~tot_depos_seas) across the study area. As expected, all members simulated the highest (lowest) ^{131}I~~conc_seas_max~~intg_conc_seas and ^{137}Cs~~depos_seas_max~~tot_depos_seas over the south (north) of Qatar, being the closest (furthest) point of the study area to the emission point. The inter-seasonal comparison of simulations shows that all ensemble members have simulated inhalation doses up to three to five times stronger in the cold period of the year in the south/southeast of Qatar than in the warm period. The examination of the air parcel release time resulting ~~in~~in the extreme ^{131}I concentrations ~~^{131}Iconc_seas_max~~ shows that they are mainly released between 5 a.m. and 12 p.m. It seems that the intensification of the thermal gradient between the land and sea and the resulting onshore winds increased the transport of high ^{131}I concentrations (inhalation doses), through freshly released air parcels, to the study area at this time of day. Among the ensemble members, the highest and lowest levels of inhalation doses, in the southeast of Qatar, ~~,~~were found in FNL and CFSv2 simulations~~,~~ respectively~~(up to 1000 µSv) and then in FNL- and ERA5 simulations (up to 600 µSv) whereas CFSv2 underpredicted inhalation doses by a factor of about 3 to 5 compared to these (re)analysis members~~. Considering that FNL and CFSv2 are executed using the same simulation code, the remarkable difference between the resulting ^{131}I~~conc_seas_max~~intg_conc_seas can be attributed to the difference in meteorological inputs. We found that the 3 to 5-fold elevated planetary boundary layer height caused the stronger dilution of radionuclides at the surface in CFSv2 simulations. In addition, the poorer spatial resolution of CFSv2 inputs than of FNL inputs caused the faulty separation of the boundary layer process along the coastlines in the former. The significant differences in ^{131}I~~conc_seas_max~~intg_conc_seas (inhalation doses) simulated by FNL and FNL-WRF show how the use of different model simulation codes (schemes) and downscaling of meteorological inputs may affect FLEXPART modeling and, consequently, the decisions made based on its simulations for real accidents. As was the case with ^{131}I~~conc_seas_max~~intg_conc_seas, ^{137}Cs~~depos_seas_max~~tot_depos_seas in the cold period of the year, especially in winter, in the south of the study area can be up to three times higher than in the warm period. The highest spread of contaminated surfaces with ^{137}Cs~~depos_seas_max~~tot_depos_seas greater than 40 kBqm−2 is found in FNL simulations. The ~~^{137}Cs~~depos_seas_max~~tot_depos_seas mostly occurred when particles are released between 10 a.m. and 2 p.m. This can be attributed to the development of the boundary layer and the increased transport of radionuclides from the source to conterminous areas at this time of the day. The examination of the frequency with which ^{131}I and ^{137}Cs concentrations above the 66^{th} percentiles are transported to the populated areas of eastern Qatar shows that, in all members, more than 50% of the extreme cases occurred in winter and between 15 and 30% in spring. The above findings show that any nuclear accident at B-NPP in the winter will be more likely to be accompanied by the transfer of high radionuclide concentrations and deposition within the study area. This pronounced intra-annual distribution could be attributed to a seasonal atmospheric pattern in which south/southeast winds transport the dense radionuclide clouds to the study area. The collocation of population density and simulations shows that the populated areas (with

more than 15 people per arc-second) coincided with moderate (less than 200 μSv and 100 kBqm^{-2}) to low levels of ^{131}I~~conc_seas_max~~intg_conc_seas (inhalation doses) and ^{137}Cs~~depos_seas_max~~tot_depos_seas ~~of less than 200 μSv and 100 kBqm^{-2}~~, respectively. Uninhabited areas in southern Qatar have received the highest levels of ^{131}I~~conc_seas_max~~intg_conc_seas and ^{137}Cs~~depos_seas_max~~tot_depos_seas. In this study, we also investigated the effect of the turbulence scheme selected under convective conditions on radionuclide dispersion. The implementation of the skewed turbulence model (STM), instead of the Gaussian one (GTM), in ERA5-WRF and FNL-WRF decreased the median of simulated ^{131}I concentrations and increased the high levels of simulated ^{137}Cs deposition. According to Pisso et al. (2019), it can be interpreted as the decline in radionuclide transport to areas away from the source due to the intensified deposition in the areas around the source under skewed turbulence conditions.

3- **The inter-comparison of ensemble members:** the outputs of CFSv2 were compared with that of three (re)analysis members. In general, CFSv2 simulations of ^{137}Cs and ^{131}I column density are most highly correlated with FNL, producing a Pearson correlation coefficient of around 0.62, and then with FNL-WRF. This is because all three members have a similar meteorological base model. The evaluation metrics including fraction bias (FB=0.02), the fraction of simulations within the factor of 5 (FB5=67.4), and normalized RMSE (NMSE=1.5) also show that CFSv2 produced the lowest absolute differences with FNL. Less than unity linear regression coefficients between CFSv2 and other members, particularly between CFSv2 and FNL ~~in spring~~, in spring show that CFSv2 caused considerable underpredictions in ^{131}I column density simulations, mainly due to the elevated input PBLH. ~~Regarding ^{137}Cs column density simulations, CFSv2 produced stronger underpredictions, but smaller absolute differences against (re)analysis members.~~ CFSv2 produced the lowest absolute difference with FNL-WRF in ^{137}Cs column density simulations (FB=~~-~~0.02, FB5=83.7, and NMSE=1.2). Considering the performance statistics between simulations from CFSv2 and reanalysis members and those computed between Xe-133 observations and simulations (Maurer et al., 2018) indicates that the uncertainty of ^{131}I and ^{137}Cs column density simulations by CFSv2 fall within the expected uncertainty range. Considering all members, the lowest absolute difference between ^{131}I and ^{37}Cs column density simulations is found between FNL-WRF and ERA5-WRF yielding FB=~~-~~0.07 and ~~-~~0.05, FB5=79.3% and 83.6%, RMSE=14.69 x 10^8 and 2946.3 x 10^7, and NMSE=1.3 and 1.1. This underlines that the use of different downscaled inputs but the same simulation code in these two members increased the similarity between resulting simulations to the extent that surpasses the association between simulations from FNL and FNL-WRF with identical meteorological inputs. The deposition simulations from all members show a larger inconsistency for both ^{131}I and ^{137}Cs. As already stated in the literature (Girard et al., 2016, Gudiksen et al., 1988, Evangeliou et al., 2017), this can be partially attributed to uncertainties in input precipitation fields and the recent updates in the wet deposition scheme of FLEXPART.

Data availability. The FLEXPART and FLEXPART-WRF simulations are available upon request. The open-source codes for the FLEXPART 10.4 and FLEXPART-WRF 3.3.2 can be downloaded from https://www.flexpart.eu/downloads (last access:

27 May 2022). Qatar's high-resolution population density datasets are freely available at https://data.humdata.org/dataset/qatar-high-resolution-population-density-maps-demographic-estimates (last access: 27 May 2022).

Author contributions. SON performed the WRF, FLEXPART, and FLEXPART-WRF simulations and led the integration of results and writing. SON and TC designed the experiments. All the co-authors have read the paper and provided professional comments.

Competing interests. The authors declare that they have no conflict of interest.

Acknowledgments.

The CyI High-Performance Computing Facility and Qatar Environment and Energy Research Institute (QEERI) High-Performance Computer provided computational resources supporting this work. The authors thank the FLEXPART and FLEXPART-WRF developers for providing the transport model source codes.

Financial support.

This research has received funding from the Qatar Environment & Energy Research Institute (QEERI), an entity of the Hamad Bin Khalifa University, wholly owned by the Qatar Foundation for Science, Education, and Community Development.

References

ARNOLD, D., MAURER, C., WOTAWA, G., DRAXLER, R., SAITO, K. & SEIBERT, P. 2015. Influence of the meteorological input on the atmospheric transport modelling with FLEXPART of radionuclides from the Fukushima Daiichi nuclear accident. *Journal of environmental radioactivity*, 139**,** 212-225.

BABUKHINA, T., GAN'SHIN, A., ZHURAVLEV, R., LUK'YANOV, A. & MAKSYUTOV, S. S. 2016. Estimating by inverse modeling the release of radioactive substances (133 Xe, 131 I, and 137 Cs) into the atmosphere from Fukushima Daiichi nuclear disaster. *Russian Meteorology and Hydrology*, 41**,** 335-343.

BRIOUDE, J., ARNOLD, D., STOHL, A., CASSIANI, M., MORTON, D., SEIBERT, P., ANGEVINE, W., EVAN, S., DINGWELL, A. & FAST, J. D. 2013. The Lagrangian particle dispersion model FLEXPART-WRF version 3.1. *Geoscientific Model Development*, 6**,** 1889-1904.

CASSIANI, M., STOHL, A. & BRIOUDE, J. 2015. Lagrangian stochastic modelling of dispersion in the convective boundary layer with skewed turbulence conditions and a vertical density gradient: Formulation and implementation in the FLEXPART model. *Boundary-Layer Meteorology*, 154**,** 367-390.

CHINO, M., NAKAYAMA, H., NAGAI, H., TERADA, H., KATATA, G. & YAMAZAWA, H. 2011. Preliminary estimation of release amounts of 131I and 137Cs accidentally discharged from the Fukushima Daiichi nuclear power plant into the atmosphere. *Journal of nuclear science and technology*, 48**,** 1129-1134.

CHRISTOUDIAS, T. & LELIEVELD, J. 2013. Modelling the global atmospheric transport and deposition of radionuclides from the Fukushima Dai-ichi nuclear accident. *Atmospheric Chemistry and Physics*, 13**,** 1425-1438.

DE VRIES, A., FELDSTEIN, S. B., RIEMER, M., TYRLIS, E., SPRENGER, M., BAUMGART, M., FNAIS, M. & LELIEVELD, J. 2016. Dynamics of tropical–extratropical interactions and extreme precipitation events in Saudi Arabia in autumn, winter and spring. *Quarterly Journal of the Royal Meteorological Society*, 142**,** 1862-1880.

EVANGELIOU, N., HAMBURGER, T., COZIC, A., BALKANSKI, Y. & STOHL, A. 2017. Inverse modeling of the Chernobyl source term using atmospheric concentration and deposition measurements. *Atmospheric Chemistry and Physics*, 17**,** 8805-8824.

FARID, M., PRAWITO, SUSILA, I. & YUNIARTO, A. Design of early warning system for nuclear preparedness case study at Serpong. AIP Conference Proceedings, 2017. AIP Publishing LLC, 030067.

FAST, J. D. & EASTER, R. C. A Lagrangian particle dispersion model compatible with WRF. 7th Annual WRF User's Workshop, 2006. Citeseer, 19-22.

GALMARINI, S., BIANCONI, R., KLUG, W., MIKKELSEN, T., ADDIS, R., ANDRONOPOULOS, S., ASTRUP, P., BAKLANOV, A., BARTNIKI, J. & BARTZIS, J. 2004. Ensemble dispersion forecasting—Part I: concept, approach and indicators. *Atmospheric Environment*, 38**,** 4607-4617.

GIRARD, S., MALLET, V., KORSAKISSOK, I. & MATHIEU, A. 2016. Emulation and Sobol'sensitivity analysis of an atmospheric dispersion model applied to the Fukushima nuclear accident. *Journal of Geophysical Research: Atmospheres*, 121**,** 3484-3496.

GRELL, G. A., PECKHAM, S. E., SCHMITZ, R., MCKEEN, S. A., FROST, G., SKAMAROCK, W. C. & EDER, B. 2005. Fully coupled "online" chemistry within the WRF model. *Atmospheric Environment*, 39**,** 6957-6975.

GRYTHE, H., KRISTIANSEN, N. I., GROOT ZWAAFTINK, C. D., ECKHARDT, S., STRÖM, J., TUNVED, P., KREJCI, R. & STOHL, A. 2017. A new aerosol wet removal scheme for the Lagrangian particle model FLEXPART v10. *Geoscientific Model Development*, 10**,** 1447-1466.

GUDIKSEN, P., HARVEY, T. & LANGE, R. 1988. Chernobyl source term, atmospheric dispersion, and dose estimation. Lawrence Livermore National Lab., CA (USA).

HANNA, S. 1982. Applications in Air Pollution Modeling. Atmospheric Turbulence and Air Pollution Modeling. *Holland*.

HERSBACH, H., BELL, B., BERRISFORD, P., HIRAHARA, S., HORÁNYI, A., MUÑOZ-SABATER, J., NICOLAS, J., PEUBEY, C., RADU, R. & SCHEPERS, D. 2020. The ERA5 global reanalysis. *Quarterly Journal of the Royal Meteorological Society*, 146**,** 1999-2049.

IAEA 2009. *Regulations for the safe transport of radioactive material*, International Atomic Energy Agency.

JIN, D. Z. & KOZHEVNIKOV, A. A. 2011. A compact statistical model of the song syntax in Bengalese finch. *PLoS computational biology*, 7**,** e1001108.

KINASE, T., ADACHI, K., SEKIYAMA, T. T., KAJINO, M., ZAIZEN, Y. & IGARASHI, Y. 2020. Temporal variations of 90 Sr and 137 Cs in atmospheric depositions after the Fukushima Daiichi Nuclear Power Plant accident with long-term observations. *Scientific reports*, 10**,** 1-8.

LEADBETTER, S. J., JONES, A. R. & HORT, M. C. 2022. Assessing the value meteorological ensembles add to dispersion modelling using hypothetical releases. *Atmospheric Chemistry and Physics*, 22**,** 577-596.

LONG, P., HIEN, P. & QUANG, N. 2019. Atmospheric transport of 131I and 137Cs from Fukushima by the East Asian northeast monsoon. *Journal of environmental radioactivity*, 197**,** 74-80.

LUHAR, A. K., HIBBERD, M. F. & HURLEY, P. J. 1996. Comparison of closure schemes used to specify the velocity PDF in Lagrangian stochastic dispersion models for convective conditions. *Atmospheric Environment*, 30**,** 1407-1418.

MARYON, R. 1998. Determining cross-wind variance for low frequency wind meander. *Atmospheric Environment*, 32**,** 115-121.

MAURER, C., BARÉ, J., KUSMIERCZYK-MICHULEC, J., CRAWFORD, A., ESLINGER, P. W., SEIBERT, P., ORR, B., PHILIPP, A., ROSS, O. & GENEROSO, S. 2018. International challenge to model the long-range transport of radioxenon released from medical isotope production to six Comprehensive Nuclear-Test-Ban Treaty monitoring stations. *Journal of environmental radioactivity*, 192**,** 667-686.

MOUSSIOPOULOS, N. 1997. *Ambient air quality, pollutant dispersion and transport models*, European Environment Agency.

NABI, S. W., HAMEED, S. N. & VANDERBAUWHEDE, W. 2015. A Reconfigurable Vector Instruction Processor for Accelerating a Convection Parametrization Model on FPGAs. *arXiv preprint arXiv:1504.04586*.

NCEP 2015. NCEP GDAS/FNL 0.25 Degree Global Tropospheric Analyses and Forecast Grids. Research Data Archive at the National Center for Atmospheric Research, Computational and Information Systems Laboratory.

PAPAGIANNOPOULOS, N., D'AMICO, G., GIALITAKI, A., AJTAI, N., ALADOS-ARBOLEDAS, L., AMODEO, A., AMIRIDIS, V., BAARS, H., BALIS, D. & BINIETOGLOU, I. 2020. An EARLINET early warning system for atmospheric aerosol aviation hazards. *Atmospheric Chemistry and Physics*, 20**,** 10775-10789.

PISSO, I., SOLLUM, E., GRYTHE, H., KRISTIANSEN, N. I., CASSIANI, M., ECKHARDT, S., ARNOLD, D., MORTON, D., THOMPSON, R. L. & GROOT ZWAAFTINK, C. D. 2019. The Lagrangian particle dispersion model FLEXPART version 10.4. *Geoscientific Model Development*, 12**,** 4955-4997.

SAHA, S., MOORTHI, S., WU, X., WANG, J., NADIGA, S., TRIPP, P., BEHRINGER, D., HOU, Y.-T., CHUANG, H.-Y. & IREDELL, M. 2011. NCEP climate forecast system version 2 (CFSv2) 6-hourly products. *Research Data Archive at the National Center for Atmospheric Research, Computational and Information Systems Laboratory*, 10**,** D61C1TXF.

SAHA, S., MOORTHI, S., WU, X., WANG, J., NADIGA, S., TRIPP, P., BEHRINGER, D., HOU, Y.-T., CHUANG, H.-Y. & IREDELL, M. 2014. The NCEP climate forecast system version 2. *Journal of climate*, 27**,** 2185-2208.

SEIBERT, P. & ARNOLD, D. A quick fix for the wet deposition cloud mask in FLEXPART. EGU General Assembly Conference Abstracts, 2013. EGU2013-7922.

SPIEGELBERG-PLANER, R. 2013. *INES: The International Nuclear and Radiological Event Scale: User's Manual*, International Atomic Energy Agency.

STOHL, A., FORSTER, C., FRANK, A., SEIBERT, P. & WOTAWA, G. 2005. The Lagrangian particle dispersion model FLEXPART version 6.2. *Atmospheric Chemistry and Physics*, 5**,** 2461-2474.

STOHL, A., HITTENBERGER, M. & WOTAWA, G. 1998. Validation of the Lagrangian particle dispersion model FLEXPART against large-scale tracer experiment data. *Atmospheric Environment*, 32**,** 4245-4264.

STOHL, A., SEIBERT, P., WOTAWA, G., ARNOLD, D., BURKHART, J. F., ECKHARDT, S., TAPIA, C., VARGAS, A. & YASUNARI, T. 2012. Xenon-133 and caesium-137 releases into the atmosphere from the Fukushima Dai-ichi nuclear power plant: determination of the source term, atmospheric dispersion, and deposition. *Atmospheric Chemistry and Physics*, 12**,** 2313-2343.

STOHL, A., SODEMANN, H., ECKHARDT, S., FRANK, A., SEIBERT, P., WOTAWA, G., MORTON, D., ARNOLD, D. & HARUSTAK, M. 2010. The Lagrangian particle dispersion model FLEXPART version 9.3. Tech. rep., Norwegian Institute of Air Research (NILU), Kjeller, Norway ….

STOHL, A. & THOMSON, D. J. 1999. A density correction for Lagrangian particle dispersion models. *Boundary-Layer Meteorology*, 90**,** 155-167.

TAKAGI, M., OHARA, T., GOTO, D., MORINO, Y., UCHIDA, J., SEKIYAMA, T. T., NAKAYAMA, S. F., EBIHARA, M., OURA, Y. & NAKAJIMA, T. 2020. Reassessment of early 131I inhalation doses by the Fukushima nuclear accident based on atmospheric 137Cs and 131I/137Cs observation data and multi-ensemble of atmospheric transport and deposition models. *Journal of Environmental Radioactivity*, 218**,** 106233.

THOMPSON, R. L., STOHL, A., ZHOU, L. X., DLUGOKENCKY, E., FUKUYAMA, Y., TOHJIMA, Y., KIM, S. Y., LEE, H., NISBET, E. G. & FISHER, R. E. 2015. Methane emissions in East Asia for 2000–2011 estimated using an atmospheric Bayesian inversion. *Journal of Geophysical Research: Atmospheres*, 120**,** 4352-4369.

TIPKA, A., HAIMBERGER, L. & SEIBERT, P. 2020. Flex_extract v7. 1.2–a software package to retrieve and prepare ECMWF data for use in FLEXPART. *Geoscientific Model Development*, 13**,** 5277-5310.

TSURUTA, H., MORIGUCHI, Y. & NAKAJIMA, T. 2019. Dynamics of atmospheric 131 I in radioactive plumes in eastern Japan immediately after the Fukushima accident by analysing published data. *Scientific reports*, 9**,** 1-15.

UNSTATS 2020. *Demographic Yearbook 2020*.

WAI, K.-M., KRSTIC, D., NIKEZIC, D., LIN, T.-H. & PETER, K. 2020. External Cesium-137 doses to humans from soil influenced by the Fukushima and Chernobyl nuclear power plants accidents: A comparative study. *Scientific reports*, 10**,** 1-8.

WHO 2012. *Preliminary dose estimation from the nuclear accident after the 2011 Great East Japan Earthquake and Tsunami*, World Health Organization.

YU, Y., NOTARO, M., KALASHNIKOVA, O. V. & GARAY, M. J. 2016. Climatology of summer Shamal wind in the Middle East. *Journal of Geophysical Research: Atmospheres*, 121**,** 289-305.

ZHANG, Z. & CHEN, Q. 2007. Comparison of the Eulerian and Lagrangian methods for predicting particle transport in enclosed spaces. *Atmospheric environment*, 41**,** 5236-5248.